工學博士學位論文

Fabrication of Palladium-decorated Polypyrrole and Graphene Electrodes for Sensor Applications

팔라듐이 도입된 폴리피롤과 그래핀 전극의 제조 및 센서로의 응용

2017年 2月

서울大學校 大學院

化學生物工學部

申 東 燻

Fabrication of Palladium-decorated Polypyrrole and Graphene Electrodes for Sensor Applications

2017年

申東燻

↑
2cm
↓

↑
2.5cm
↓

↑
4cm
↓

↑
3cm
↓

↑
2cm
↓

Fabrication of Palldium-decorated Polypyrrole and Graphene Electrodes for Sensor Applications

팔라듐이 도입된 폴리피롤과 그래핀 전극의 제조 및 센서로의 응용

指導敎授 張 正 植

이 論文을 工學博士 學位論文으로 提出함
2016 년 11 월
서울大學校 大學院
化學生物工學部
申 東 燻

申東燻의 工學博士 學位論文을 認准함
2016 年 11 月

委 員 長 _____ (인)
副委員長 _____ (인)
委 員 _____ (인)
委 員 _____ (인)
委 員 _____ (인)

Fabrication of Palladium-decorated Polypyrrole and Graphene Electrodes for Sensor Applications

by

Dong Hoon Shin

Submitted to the Graduate School of Seoul National University in Partial Fulfillment of the Requirements for the Degree of Doctor of Philosophy

February, 2017

Thesis Adviser: Jyongsik Jang

Abstract

There has been tremendous research for the devolopment of novel materials with excellent properties and performances. In particular, composite materials, consist of inorganic and organic component, not only display synergetic effect between inorganic (high performance) and organic (high stability) but also meet the economic and environmental demands. Among them, palladium contained carbon-based composite materials have attracted enormous attention in research and industry fields due to the high hydrogen reactivity and catalytic performance. Although blending technique of inorganic nanomaterials as filler and carbon materials already applied for various part, there is still lack of investigation on the decoration of inorganic materials on the carbon materials.

This dissertation demonstrates that polypyrrole/polyacrylonitrile nanofibers using electrospinning and VDP (vapor deposition polymerization) and graphene thin layer using CVD (chemical vapor deposition) were fabricated as conductive substrates, and then, composite materials based on palladium nanostructure synthesized *via* electrodeposition process. These synthesized composite materials present improved electric and chemical properties, enabling to be

applied for various sensor applications. When introduced to transducer materials for sensor device, it provides the fast response and high stability owing to the synergetic effect. In addition, increasing surface area from controllable palladium nanostructure induces the amplified interaction with target materials and facilitates realization of the high sensitive sensor.

Keywords: palladium, polypyrrole, graphene, field-effect-transistor, sensor

Student Number: 2014-30255

List of Abbreviations

-NH_2: amino group

1D: one-dimension

2D: two dimension

3D: three dimension

A: ampere

Ag/AgCl electrode: silver chloride electrode

Ag: silver

Au: gold

BPd_PPy/PAN NFs: blunt palladium nanoparticles-decorated polypyrrole/polyacrylonitrile nanofibers

ca.: circa

CH_4: methane

cm: centi-meter

CPs: conducting polymers

Cu: copper

CVD: chemical vapor deposition

D: drain

DAN: 1,5-diaminonaphthalene

DMF: dimethyl formamide

e^- :electron

eV: electron volt

fcc: face-centered-cubic

FE-SEM: field emission-scanning electron microscopy

$FeCl_3$: iron (III) chloride

FET: field-effect-transistor

FPNCs_CG: flower-like palladium nanoclusters-decorated CVD graphene

FT-IR: fourier transform-infrared

GCE: glassy carbon electrode

GO: graphene oxide

GOH: 3D graphene oxide hydrogel

GOx: glucose oxidase

H_2: hydrogen

H_2O_2: hydrogen peroxide

H_2S: hydrogen sulfide

H_2SO_4: sulfuric acid

HIV: human-immunodeficiency-virus

HR-TEM: high resolution-transmission electron microscopy

hr: hour

I-V: current-voltage

I: instantaneous recorded current

I_0: initial current

I_{SD}-V_{SD}: source-drain current versus source-drain voltage

I_{SD}: source-drain current

k_{-1}: desorption constant

k_1: adsorption constant

M: mole

MCs: mesoporous carbons

MDL: minimum detectable level

MFC: mass flow controller

min: minute

mM: milli-mole

N_2: nitrogen

NaOH: sodium hydroxide

nm: nano-meter

nM: nano-mole

NO_2: nitrogen dioxide

p-type: positive-type

p: partial pressure

PA: polyacetylene

PAN: polyacrylonitrile

PANI: polyaniline

PBS: phosphate-buffered saline

$Pd(OH)_2$: palladium hydroxide

Pd: palladium

$PdCl_2$: palladium (II) chloride

PdHx: palladium hydride

PdO: palladium oxide

PEDOT: poly(3,4-ethylenedioxylthiophene)

PEN: polyethylene naphthalate

PMMA: poly(methyl methacrylate)

ppm: parts per million

PPy/PAN NFs: polypyrrole-coated polyacrylonitrile nanofibers

PPy: polypyrrole

PSe: polyselenophene

Pt: platinum

PT: polythiophene

r: adsorption rate

R_0: initial resistance

rGO: reduced graphene oxide

S/N: signal to noise

s: second

S: source or sensitivity

sccm: standard cubic centimeters per minute

slm: standard liters per minute

SnO_2: tin dioxide

SO_4^{2-}: sulfate ion

SPd_PPy/PAN NFs: sharp palladium-decorated polypyrrole-coated polyacrylonitrile nanofibers

SPNFG: shape-controlled palladium nanoflower-decorated CVD graphene

SWNT: single wall nanotube

TEM: transmission electron microscopy

V: voltage

VDP: vapor deposition polymerization

V_G: gate voltage

XPS: x-ray photoemission spectroscopy

XRD: x-ray diffraction

ΔR: resistance change

θ: fraction of metal covered by target gas

μm: micro-meter

List of Figures

List of Tables

Table of Contents

1. Introduction

1.1 Background

1.1.1 Conducting Polymers

Conducting polymers (CPs) are attractive materials from both fundamental and practical point of view. Since the discovery of polyacetylene (PA) doped with halogens in 1977, diverse types of CPs such as polypyrrole (PPy), polyaniline (PANI), polythiophene (PT), polyselenophene (PSe), poly(3,4-ethylenedioxylthiophene) (PEDOT) and their derivatives have been developed and received considerable attention (**Figure 1**) due to the CPs characteristic derived from polyconjugated backbone consisting of alternating single (σ) and double (π) bonds [1-4]. Furthermore, CPs have the magnetic and optical properties of metals and semiconductors while maintaining the high mechanical properties and processing merits of polymers [5,6].

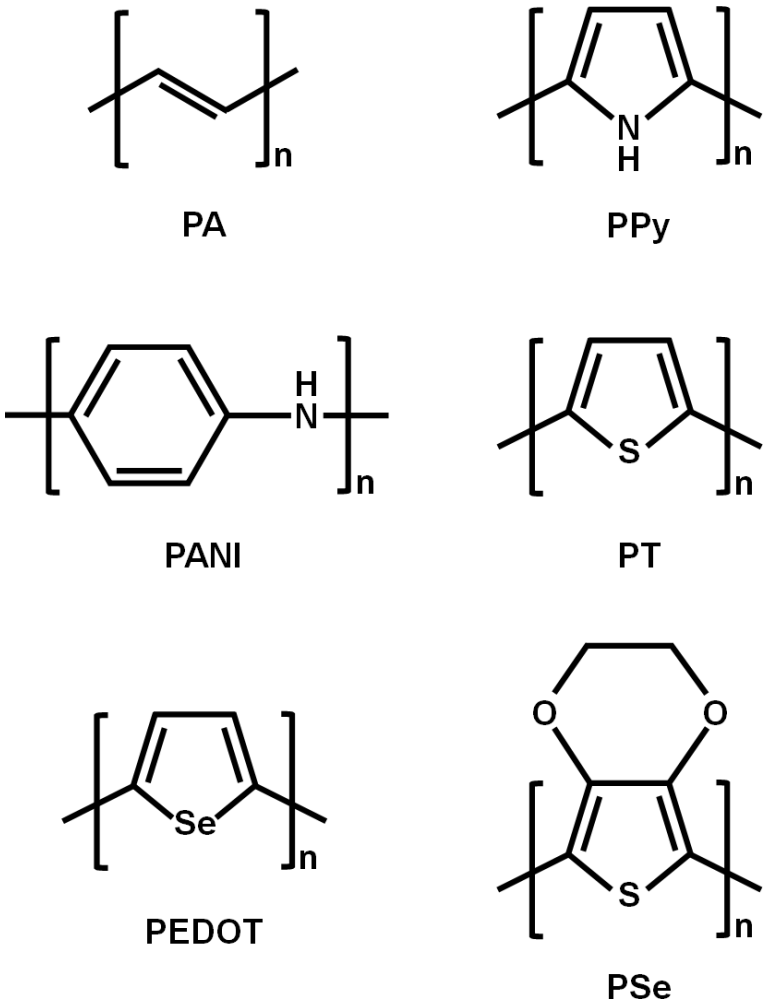

Figure 1. Various conducting polymer structures [2].

1.1.1.1 Polypyrrole

Among other conducting polymers, PPy which composed of five-membered heterocyclic rings provides the valuable properties including high electrical conductivity, interesting redox characteristic and good environmental stability [7,8]. PPy is generally prepared by chemical or electrochemical method. Chemical synthesis is used to obtain the large quantities (powder) and it was required for an oxidant (*e.g.* $FeCl_3$) with a Py monomer. On the other hand, electrochemical synthesis is employed for certain purpose (film) owing to the simplicity, control of materials condition (thickness, location, dopant type) [9-11].

Although the repeat unit of PPy is dominantly composed of α-α coupling (linear chain structure), various steric and structural defect (α-β bonds, carbonyl and hydroxyl group) is occurred during polymerization method (**Figure 2**). These defects induce irregular sturucture (disorder) and decrease conductivity of polymer [12].

Figure 3 presents the energy diagram of PPy with four different electronic band structure. According to the oxidation of PPy, radical cations (polarons) generates due to the removal of π-electron from valance band (neutral state). These polarons introduce the two new

energy level within the bandgap. Bipolarons which are the charge carriers of the coupled cations (dication) generate under the further oxidation. **Figure 4** indicated that intermediate band structure formed because the overlap between bipolaron is happened by additional oxidation of bipolarons [13,14].

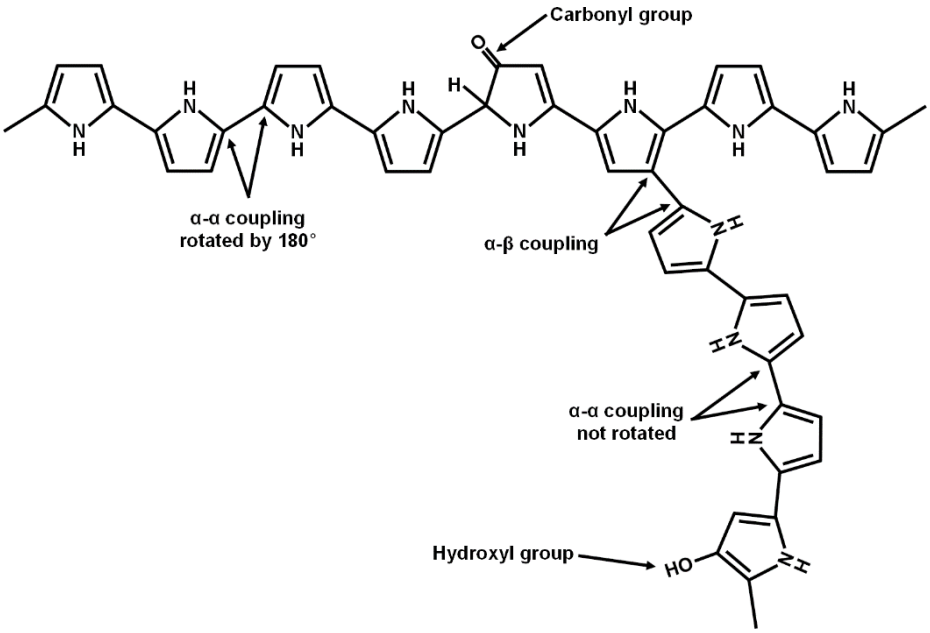

Figure 2. Possible chemical structures in PPy chains [8].

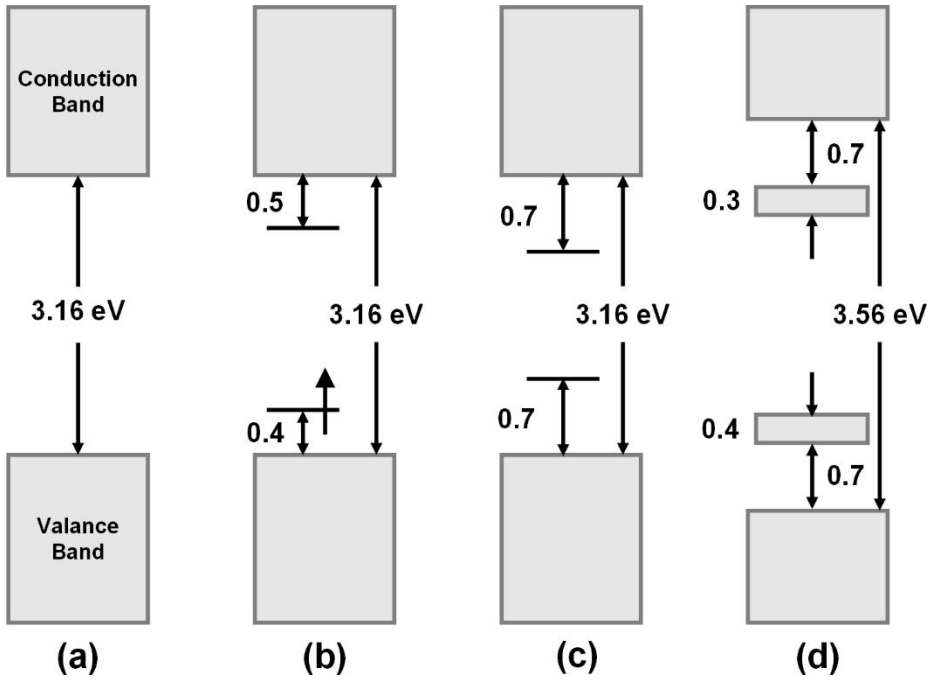

Figure 3. Electronic energy diagrams for (a) neutral (b) polaron, (c) bipolaron, and (d) fully doped PPy, respectively [10].

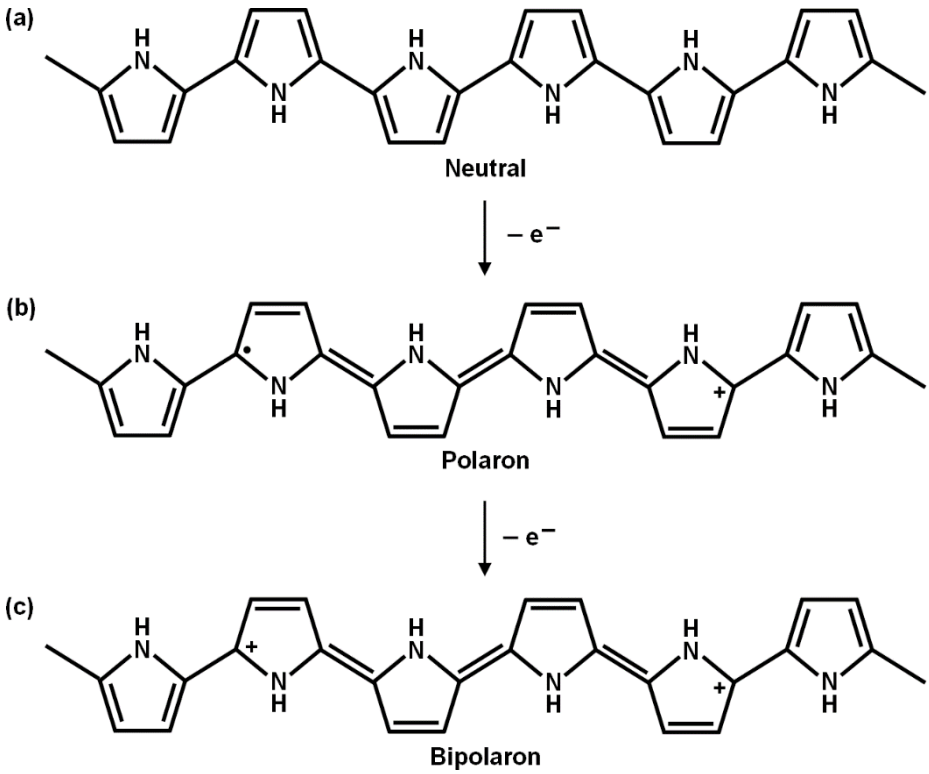

Figure 4. Structure for (a) neutral, (b) polaron, (c) bipolaron PPy, respectively [10].

1.1.1.2 1D nanomaterials

Over the past decade, nanotechnology is essential field of research due to the enormous potential for a various applications. There are four types of nanostructure such as zero, one, two, and three dimension structure. Aomong them, one-dimensional (1D) nanostructures is specially promising structure because of their unique physical and chemical properties as presented in **Figure 5** [15-17]. Compared to the other dimensional materials, 1D nanostructure is the smallest dimensional structure and high aspect ratio which provides the outstanding charge carrier mobility along the axial direction. Various synthetic methods such as template-directed, electrospinning, solvothermal, self-assembly method have been exploited [18].

1.1.1.2.1 Electrospinning method

Electrospinning is one of the most effective technique to fabricate the 1D nanostructure and has been attracted much attention due to the consistant in produing fibers within micron range [19-21]. Polymer nanofibers are fabricated by evaporation of solvent in polymer solution under high voltage electric field. The highly charged fibers are gathered directly toward opposite charged collector. As a result, the spinning

fibers are achieved by the tensile force generated in the axial direction of the polymer flow by the induced charges in electric field (**Figure 6**). These electrospun fibers, which have smaller pores and high surface area, can be widely applied in various application such as nanocatalyst, bioengineering, sensor, optical electronics, *etc* [22,23].

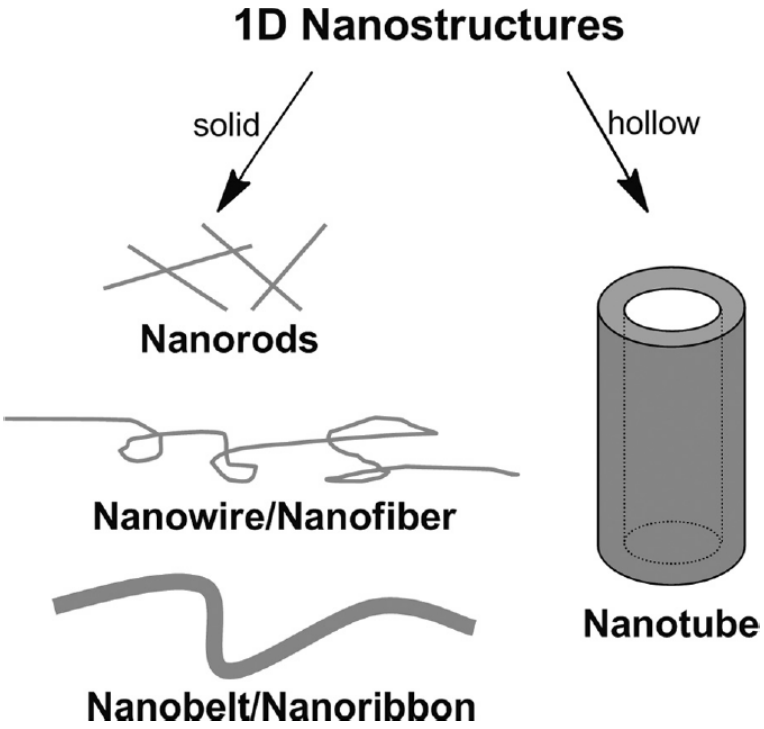

Figure 5. Solid and hollow 1D nanostructures of conducting polymers [18].

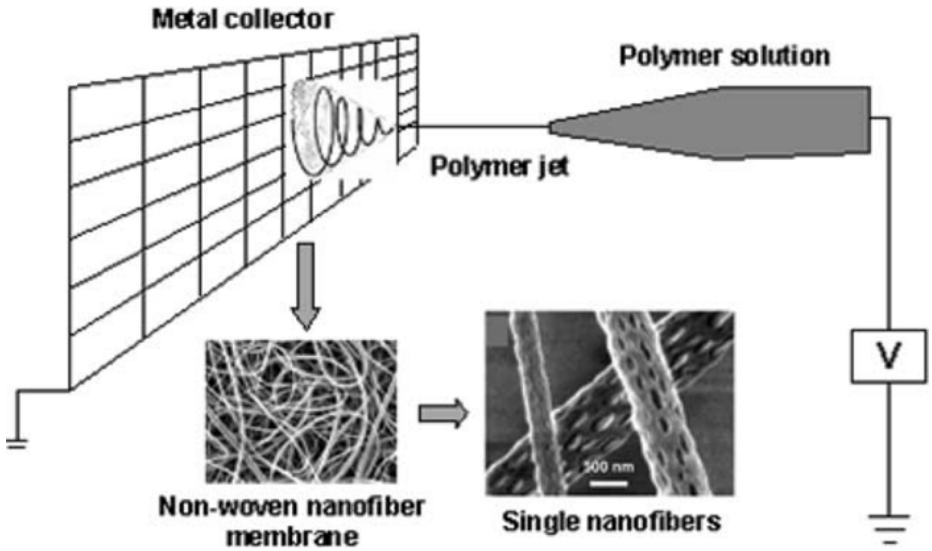

Figure 6. Schematic diagram for fabrication of polymer nanofibers by electrospinning [19].

1.1.2 CVD graphene

Graphene, a two-dimensional materials with honeycomb structure composed of single- or few- layer sheet of sp^2-hybridized carbon atoms, has been attracting much attention owing to the unique physical, mechanical, electrical properties [24-26]. Chemical exfoliation, mechanical exfoliation, epitaxial growth, and CVD graphene is widely used method to prepare the graphene. Among these graphene synthesis approaches, CVD graphene is one of promising materials due to high mobility, tunable bandgap, quantum electronic transport, and thermal stability [27]. During the CVD process, gas species containing the hydrocarbon are introduced into the hot reactor, and then, form the graphene sheet on the metal substrate (**Figure 7**). These metal substrate acts as catalyst to lower the energy barrier (**Figure 8**). Single-layer CVD graphene typically used to flexible transparent conductor or FETs for biosensing [28-30].

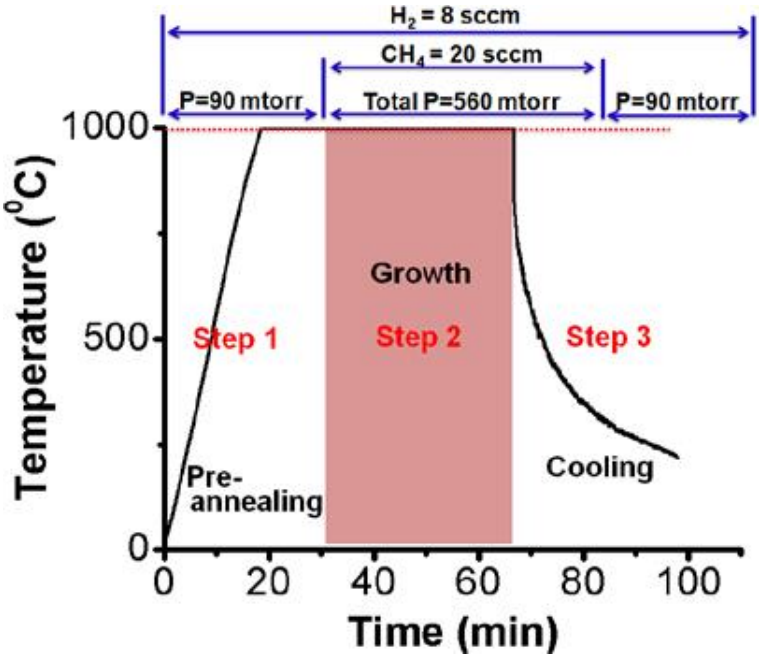

Figure 7. Time dependence of experimental parameters: temperature, pressure, and gas composition/flow rate [28].

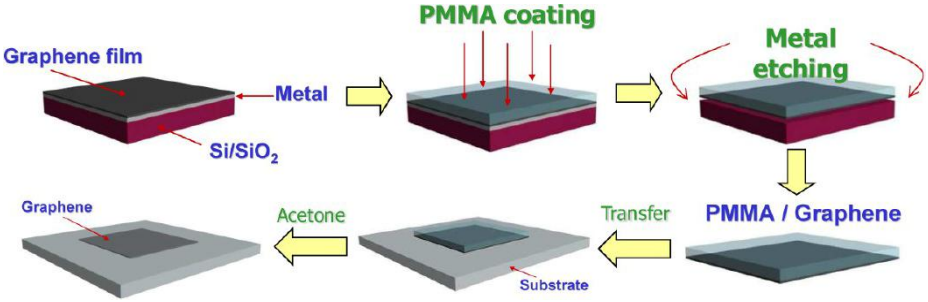

Figure 8. Schematic diagram of the transfer process [28].

1.1.3 Noble metal

Noble metals such as gold (Au), silver (Ag), platinum (Pt), and palladium (Pd) have been received tremendous attention due to the unique and tunable electrical, chemical, and optical characteristic in various application fields [31-35]. Among the noble metals, Pd plays a pivotal role in many research and industrial application [36,37]. This is because Pd serves as not only primary catalyst for organic reaction but also storage or sensing materials toward hydrogen. Two representive method (bottom-up and top-down methods) is typically used to synthesize the noble metals. First, bottom-up approach which is based on reducing the metal ions includes chemical, electrochemical, and thermal reduction method [38,39]. On the other hand, top-down technique based on lithography accompanied with elimination step of bulk substrate [40,41].

1.1.4 Composite materials

In general, inorganic materials in nanoscale exhibit limitation such as aggregation by Oswald repening and volume exchange by oxidation-reduction mechanism. On the other hand, organic materials display the higher stability, however, lower performance compared to inorganic materials. Therefore, composite materials at sizes ranging from a few nanometers to several micro- to milli-meters is considered one of the most promising material categories in the material science fields [42,43]. They have unique possibilities to generate the mutual supplementation properties by synergetic combination of inorganic and organic materials. These composite approach by the selection of the well-matched components provides breakthrough to solve numerous technical problems [44,45].

1.1.4.1 Noble metal/Conducting polymer

Noble metal/Conducting polymer nanocomposites offer interesting structures to examine the potential of designing device functionality and display improved sensing and catalytic abilities compared to conducting polymer [46,47]. To prepare the Noble metal/Conducting polymer nanocomposites, there are two approaches: 1) the surface of

preformed conducting polymer is connected with metal ions, and then, metal nanoparticles deposited on the surface of conducting polymer [48]. 2) conducting polymer which is polymerized with preformed metal nanoparticles *via* chemical oxidative polymerization process leads to the formation of Noble metal/Conducting polymer nanocomposites [49].

1.1.4.2 Noble metal/CVD graphene

Hybrid materials composed of noble metal and CVD graphene composite materials have attracted considerable interest due to their various applications [50,51]. From a hybrid material point of view, CVD graphene as support material plays an important roles in determining the catalytic property and stability. Compared to the other carbon derivative, CVD graphene as a two-dimensional single layer honeycomb structure is regarded as an effective inorganic materials support materials due to the high surface area, electrical conductivity, thermal/chemical stability, and strong adhesion [52,53]. These properties appropriate for dispersion of nano-sized inorganic material which facilitates the charge transport at the graphene surface.

1.1.4.3 Electrodeposition method

To fabricate the composite materials, there are various method such as thermal reduction (autoclave), microwave, and electrodeposition [54-57]. Among them, electrodeposition is a surface coating technique which uses electric current to reduce metal cations in electrolyte, and then, they create metal or its oxide on a conductive substrate [58,59]. Differ from the conventional method which simply coated on conductive substrate to form a film shape, recently, variety shape of materials are synthesized using photolithography or fucnaionalization of conductive substrate surface, and controlling the diffusion rate of cation ion in electrolyte (**Figure 9**).

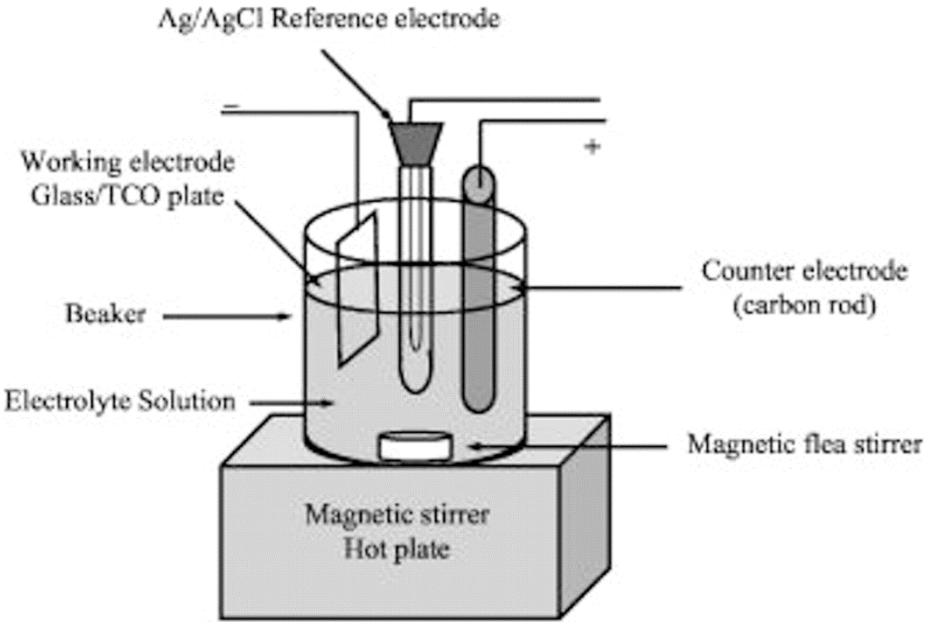

Figure 9. Schematic diagram of electrodeposition process [59].

1.1.5 Sensor applications

Sensor composed of active sensing materials and signal transducer is device to detect environmental change. Most important role of sensor device is sensitive response toward external stimulation and transport of accurate signal without noise or amplification [60-62]. These sensor is classified to chemical and biosensor according to the target analyte. The chemical sensor is analysis tool that provides the information of chemical composition toward gas-type analyte [63]. On the other hand, biosensor is device to detect the biological component contained analyte. To construct an effective sensing system, they need to high sensitivity, selectivity of target component, low operating temperature, and long-term stability [64-66].

1.1.5.1 Chemical Sensor

Within the area of chemical sensor, resistive chemical sensor, which is called chemiresistive sensor, is based on the detection of electrical resistance change by interaction between chemical component and active materials [67-69]. The target analytes are typically hydrogen sulfide (H_2S), nitrogen dioxide (NO_2), and hydrogen (H_2), *etc.* Mechanism that detects these analytes are withdrawing or donaing of

electron, and phase change of materials [70-72].

1.1.5.1.1 H_2 gas sensor

Hydrogen (H_2) gas is used extensively in many industrial processes and is an essential fuel source in clean-energy transportations and power generation applications [73,74]. However, it is highly flammable and explosive at volume concentrations higher than *ca.* 4 %. Therefore, hydrogen sensors that have high sensitivity, rapid response, and reversibility are required to detect and/or monitor minute hydrogen leakages in industrial applications [75,76]. In general, commercial hydrogen sensors composed of metal oxide (SnO_2) films meet these demand but require an operating temperature of over 200 °C, which increases the overall power consumption of the sensing device [77-79].

1.1.5.2 Liquid-ion-gated FET-type biosensor

Biosenors based on detection of biological sensing agent such as antibody, cell, receptor, and aptamers are binded to funtionalized conductive materials (tranducer). Field-effect-transistors (FETs) is attracted tremendous interest as one of the biosensor cadidates due to potential of achieving high current amplification and displaying an improved signal-to-noise (S/N) ratio [80-82]. Particularly, graphene with outstanding physical, chemical, and electrical properties are appropriated for biosensor application. Graphene based FETs for biosensor could convert from biological-recognition to electrical signal owing to the directly exposure of target analyte. Because reduced graphene oxide (rGO) can be easily prepared with numerous functional group, graphene based biosensor generally is employed using rGO [83]. Moreover, CVD graphene has attracted much attention due to the aggregation-free and uniformity opposited to rGO as represented in **Figure 10** [84,85].

1.1.5.2.1 H_2O_2 sensor

Hydrgen peroxide (H_2O_2) is not only a reactive oxygen species related to fatal disease including atherosclerosis, HIV, and Alzheimer but also a

by-product of oxidative bio-connected reactions such as glucose oxidase, galactose oxidase, saecosine oxidase, *etc* [86-90]. Therefore, detection of H_2O_2 with high sensitivity and long-term stability is an essential part for pharmaceutical, clinical, food analysis, environmental monitoring [91]. To detect the H_2O_2, numerous effort such as infrared, RAMAN, mass spectroscopy, electrochemical, and colorimetric method [92-94]. Among them, electrochemical technique toward H_2O_2 is attracted tremendous attention due to the high sensitivity and specificity.

1.1.5.2.2 Glucose sensor

Diabetes mellitus is a disturbance of the metabolism that affects many people worldwide; it is caused by insulin deprivation or hypoglycemia [95-97]. This disease is accompanied by serious complications (blindness, renal or cardiac insufficiency), that are related to poor blood circulation, and gangrene that may require amputate [98,99]. Because the glucose level in blood, urine, and body fluids is a crucial indicator for the detection of diabetes mellitus, high sensitive glucose sensor is essential devices in medical diagnosis and management [100]. Various approaches have been explored to detect glucose. These include electrochemical (amperometry, potentiometry) and optical (Raman

spectroscopy, infrared spectroscopy and surface plasmon resonance) methods [101-105]. From among these methods, the electrochemical technique has attracted the most interest due to the simple device configuration, high sensitivity and reliability, low detection limit, and cost-effectiveness [106-109].

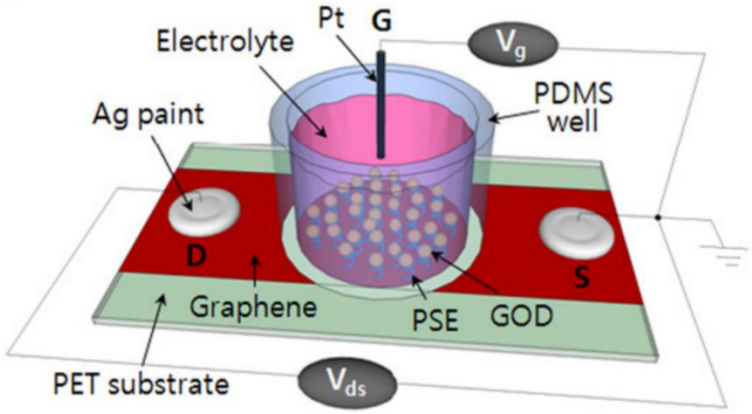

Figure 10. FET sensor based on CVD graphene; experimental apparatus of the solution gated CVD graphene sensor [85].

1.2 Objectives and Outlines

1.2.1 Objectives

The aim of this dissertation is proposing novel method to fabricate palladium-decorated composite materials for highly sensitive sensor application. Various condition contolled palladium such as shape, population, and sharpness were introduced to manufacture the sensor electrode. Polypyrrole (PPy)/polyacrylonitrile (PAN) nanofibers and chemical vapor deposition (CVD)-grown graphene as conductive substrate were adoped for palladium decoration. According to the facile synthesis methods in each condition, the palladium-decorated composite materials can be obtained with enhanced and outstanding properties. These as-prepared palladium-decorated composite materials applied to several chemical/bio sensor applicatios such as hydrogen (H_2), glucose, and hydrogen peroxide (H_2O_2), respectively.

1.2.2 Outlines

This dissertation focused on the fabrication of palladium-decorated composite materials their applications in sensor field. From fabrication of palladium-decorated hybrid materials and their sensor application field points, this dissertation involves the following subtopic:

I. Shape-controlled palladium nanoparticles-decorated PPy/PAN nanofibers electrode

I-1. Fabrication of shape-controlled palladium nanoparticles-decorated PPy/PAN NFs electrode

I-2. Application for FET-type H_2O_2 sensor

II. Population-controlled flower-like Pd NCs-decorated CVD graphene electrode

II-1. Fabrication of population-controlled flower-like Pd NCs-decorated CVD graphene electrode

II-2. Application for hydrogen sensor

III. Sharpness-controlled Pd nanoflower-decorated CVD graphene electrode

III-1. Fabrication of sharpness-controlled Pd nanoflower-decorated CVD graphene electrode

III-2. Application for selectivity-improved FET-type glcose sensor

2. Experimental Details

2.1 Fabrication of shape-controlled Pd NPs-decorated PPy/PAN NFs electrode for FET-type H_2O_2 sensor

2.1.1 Fabrication of PPy/PAN NFs

Polyacrylonitrile (PAN) powder was dissolved in dimethyl formamide (DMF) at 70 °C for 4 hr, and then, PAN NFs were electrospun from the PAN/DMF solution (10 wt %). In the electrospinning, the solution was injected through a stainless steel needle at a 10 μl/min; it was connected to a high-voltage power supply (Nano NC 15 kV). As a result, PAN NFs were consistently flowed out to the collector. The collected PAN NFs were immersed into $FeCl_3$/deionized-water solution. Fe ion-absorbed PAN NFs were then exposed to pyrrole monomer vapor in vacuum atmosphere to form the PPy/PAN NFs.

2.1.2 Fabrication of shape-controlled Pd_PPy/PAN NFs

Shape-controlled Pd NPs-decorated PPy/PAN NFs were synthesized *via* electrodeposition with or without sulfuric acid in electrolyte using

3-electrode system consist of the PPy/PAN NFs as working electrode, a platinum as counter electrode, and a Ag/AgCl as reference electode. A constant voltage (-0.1 V) was applied for 10 min to deposit Pd nanoparticles. After electrodeposition, the sample was carefully washed with destilled water and then dried at 60 °C for 1 hr in oven.

2.1.3 Characterization of shape-controlled Pd_PPy/PAN NFs

Field Emission-Scanning Electron Microscope (FE-SEM) images were obtained using a JEOL 6700 instrument. JEOL JEM-200CX and -3010 instruments were acquired for Transmission Electron Microscopy (TEM) and High Resolution-Transmission Electron Microscopy (HR-TEM), respectively. X-ray Photoemission Spectroscopy (XPS) and X-Ray Diffraction (XRD) experiments investigate on a JPS-9000MS (JEOL, Mg Kα X-ray source) and M18XHF-SRA (Rigaku, SmartLab, λ = 1.5418Å) instruments, respectively. RAMAN spectra was measured on an FRA 1106/S FT-Raman (Bruker) spectrometer and excited with a 514-nm Ar laser. The electrical properties and sensing performance of the Pd_PPy/PAN NFs were recorded using a current-source meter (Keithley 2400). *I–V* characteristics were determined using a WBCS 3000 potentiostat (WonA Tech).

2.1.4 Electrical measurement of shape-controlled Pd_PPy/PAN NFs electrode

All electrical properties were measured with a kiethley 2612A sourcemeter and probe station (MS TECH, Model 4000) and a Wonatech WBCS 3000 potentiostat. A solution chamber (volume: 200 μl) was fabricated and used to utilize the solution-based FET-type sensor. The current change is normalized as follows:

$$\left[\frac{\Delta I}{I_0}\right]_{SD}(\%) = \frac{(I - I_0)}{I_0} \times 100$$

where, I_0 is the initial current and I is the instantaneous recorded current.

2.2 Fabrication of population-controlled flower-like Pd NCs-decorated CVD graphene electrode for ultrasensitive and flexible H_2 gas sensing

2.2.1 Fabrication of CVD graphene on the flexible film

Graphene was synthesized by chemical vapor deposition (CVD) on copper (Cu) foil in a CH_4/H_2 atmosphere. The Cu foil was placed in the furnace chamber and H_2 gas was introduced at a flow rate of 8 sccm and a pressure of 147 mTorr for 30 min to stabilize the gas flow. The furnace was then heated at 40 °C min^{-1} to 1000 °C and held for 30 min. CH_4 gas was introduced at 20 sccm and 560 mTorr and the chamber was cooled to room temperature after 30min. After the surface of the graphene was coated using PMMA solution, the Cu foil and associated impurities were removed using a copper etchant, 0.01 M sulfuric acid (H_2SO_4), and distilled water, respectively. Finally, the graphene was transferred to a flexible polyethylene naphthalate (PEN) film and dipped into the acetone solution at 60 °C for 2 hr to elliminate the PMMA.

2.2.2 Fabrication of population-controlled FPNCs_CG

Electrolyte for the electrodeposition of FPNCs was prepared by dissolving 0.1 M $PdCl_2$ into 100 mL of 0.05 M H_2SO_4. Prior to electrodeposition, as-prepared CVD graphene piece (1.5 cm× 1.5 cm) was immersed in a methanolic solution containing a certain concentration (0.01, 0.1 and 1 M) of DAN (1,5-diaminonaphthalene) for 30 min. The concentration of DAN was used as the variable in controlling the population of deposited FPNCs. The electrodeposition process was conducted with a three-electrode system: the DAN-treated CVD graphene was used as the working electrode with a Ag/AgCl reference electrode and a Pt foil counter electrode. Pd was deposited by applying a constant potential of -0.1 V for 10 min. Then, the gold electrodes were deposited on the FPNCs_CG by thermal evaporation.

2.2.3 Characterization of population-controlled FPNCs_CG

Field Emission-Scanning Electron Microscope (FE-SEM) images were obtained using a JEOL 6700 instrument. JEOL JEM-200CX and JEOL JEM-3010 instruments were used for Transmission Electron

Microscopy (TEM) and High Resolution-Transmission Electron Microscopy (HR-TEM), respectively. Samples were dispersed in ethanol and cast onto perforated carbon grids. X-ray Photoemission Spectroscopy (XPS) and X-Ray Diffraction (XRD) experiments were performed on a JPS-9000MS (JEOL, Mg Kα X-ray source) and M18XHF-SRA (Rigaku, SmartLab, λ = 1.5418Å) instruments, respectively. RAMAN spectra was recorded on an FRA 1106/S FT-Raman (Bruker) spectrometer and excited with a 514-nm Ar laser. Samples for RAMAN spectroscopy were prepared on silicon-oxide-treated silicon wafers. The electrical properties and sensing performance of the FPNC_CG films were investigated using a current-source meter (Keithley 2400). *I–V* characteristics were determined using a WBCS 3000 potentiostat (WonA Tech). Fourier-Transform InfraRed (FT-IR) spectra was acquired using a Frontier FT-IR spectrometer (Perkin Elmer Inc.).

2.2.4 Electirical measurement of population-controlled FPNCs_CG electrode

Resistance changes in the FPNC_CG films toward hydrogen (H_2) were monitored with a source meter connected to a computer. The

FPNC_CG sensors were placed in a vacuum chamber within a vapor inlet/outlet pressure of 100 Torr. H_2 gas at various concentrations (0.1 – 100 ppm) was introduced into the chamber using a mass flow controller (MFC, KNH Instruments). The real-time resistance was measured at a constant applied current of 10^{-4} A. After exposure, the H_2 gas was removed by blowing across the FPNC_CG film with compressed air (N_2). This process was repeated several times. H_2 gas/N_2 air mixtures were supplied at various flow rates of 1 – 5 sccm and 2 – 8 slm using a MFC controller.

2.3 Fabrication of sharpness-controlled Pd nanoflower-decorated CVD graphene electrode for selectivity-improved FET-type glucose sensor

2.3.1 Fabrication of CVD graphene

Graphene was grown by CVD on Cu foil (25 μm-thick). In detail, the Cu foil was located in the chamber and heated to 1000 °C at a pressure of 147 mTorr gas (H_2) and a flow rate of 8 sccm. This condition was held for 30 min to stabilize the chamber atmosphere. Methane (CH_4) gas as the carbon source was then introduced at a flow rate of 20 sccm and a pressure of 560 mTorr for 30 min. Thereafter, the furnace chamber was cooled at 40 °C min^{-1} to room temperature. For the transfer process, the surface of the as-grown CVD graphene was coated with PMMA solution to protect the graphene during the transfer process, then, the PMMA-coated CVD graphene was floated on copper etchant and washed with distilled water. After transferring the PMMA-coated CVD graphene from the water to the substrate, the PMMA was removed by dissolving in acetone at 60 °C for 2 hr.

2.3.2 Fabrication of sharpness-controlled PNFG

A piece of as-grown CVD graphene (1.5 cm x 1.5 cm) was dipped into a methanol solution of DAN (1 M) for 30 min to functionalize the graphene surface. The functionalized CVD graphene was immersed in a 0.1 M $PdCl_2$ electrolyte containing various concentrations of H_2SO_4 (0.01, 0.1 and 1 M). An electrodeposition process was used to synthesize SPNFGs at room temperature using a three electrode system composed of functionalized CVD graphene as the working electrode, a Pt wire as the counter electrode, and a Ag/AgCl electrode as the reference electrode. A constant voltage (-0.1 V) was applied for 10 min to reduce from Pd^{2+} to Pd^0 on the surface of the functionalized CVD graphene. It was finally cleaned with distilled water.

2.3.3 Characterization of sharpness-controlled PNFG

Field Emission-Scanning Electron Microscope (FE-SEM) images were acquired using a JEOL 6700 instrument. JEOL JEM-2100 and JEOL JEM-3010 instruments were performed for Transmission Electron Microscopy (TEM) and High Resolution-Transmission Electron Microscopy (HR-TEM) operated at 200 kV and 300 kV installed at the National Center for Inter-university Research Facilities

at Seoul National University, respectively. X-ray Photoemission Spectroscopy (XPS) conducted on a JPS- 9000MS (JEOL, Mg Kα X-ray source).

2.3.4 Electrical measurement of sharpness-controlled PNFG electrode

All electrical measurements were performed with a Keithley 2612A sourcemeter and probe station (MS TECH, Model 4000) and a Wonatech WBCS 3000 potentiostat. To utilize the solution based sensor device, a solution chamber was (200 μl volume) was designed and used. The change in current was normalized as $[\Delta I/I_0]_{SD}$ $(\%) = [(I - I_0)/I_0]$ x 100, where I_0 is the initial current and I is the instantaneous current.

3. Results and Discussions

3.1. Fabrication of shape-controlled Pd NPs-decorated PPy/PAN NFs electrode for FET-type H_2O_2 sensor

3.1.1 Fabrication of shape-controlled Pd_PPy/PAN NFs

Figure 11 displays the overall step for the fabrication of shape-controlled palladium (Pd) NPs-decorated electrospun polypyrrole (PPy)/ polyacrylonitrile (PAN) NFs *via* electrospinning, vapor deposition polymerization (VDP) and electrodeposition. First, a PAN solution was electrospun onto the collector at a constant voltage to obtain the PAN NFs with *ca.* 180 nm as starting materials as shown in **Figure 12a and b** [110-112]. The electrospun PAN NFs were soaked into $FeCl_3$ contained aqueous solution. Fe cations are then adsorbed on the PAN NFs surfaece due to the charge-charge interaction between Fe^{3+} ions and the partial negative charge of the nitrogen atoms in the PAN structure. The surface of Fe cations adsorbed PAN NFs was exposed to pyrrole monomer vapor in vacuum system at room temperature [113,114]. Polypyrrole is coated on the PAN NFs surface with thickness of *ca.* 10 nm *via* chemical oxidation polymerization

and aggregation-free of coated PPy was attributed to the uniformly adsorption of Fe cations on the PAN NFs surface (**Figure 12c and d**). To decorate shape-controlled Pd nanoparticle on the PPy surface, PPy/PAN NFs as working electrode were immersed in a $PdCl_2$ contained aqueous solution in 3-electrode system (Ag/AgCl as the reference electrode and Pt wire as the counter electrode). When applying a constant voltage, the electrons release from the PPy surface to the Pd^{2+} from nearby in bulk solution; these electrons reduced Pd^{2+} to Pd nanoparticle [115,116]. The shape of decorated Pd nanoparticle is controlled by presence of sulfuric acid or not in electrolyte. When there is no sulfuric acid, blunt Pd (BPd) nanoparticle is decorated on the PPy surface (**Figure 13a**). On the other hand, sharp Pd (SPd) nanoparticle can be formed at presence of sulfuric acid (**Figure 13b**). This is because sulfate ion (SO_4^{2-}) prevents the growth of Pd, specially (111) plane, which is maximized this hindering effect [117,118]. The TEM images of SPd_PPy/PAN NFs represent that the SPd is *ca.* 200 nm in size and it was embbeded in PPy structure rather than attached on the surface (**Figure 13c**). Moreover, HR-TEM images of the SPd indicate an interplanar spacing of 0.224 and 0.195 nm for the (111) and (200) planes, respectively, corresponding to the face-centered-

cubic (fcc) Pd (**Figure 13d**). The blunt and sharp Pd nanoparticle-decorated PPy/PAN NFs are denoted as BPd_PPy/PAN NFs and SPd_PPy/PAN NFs, respectively.

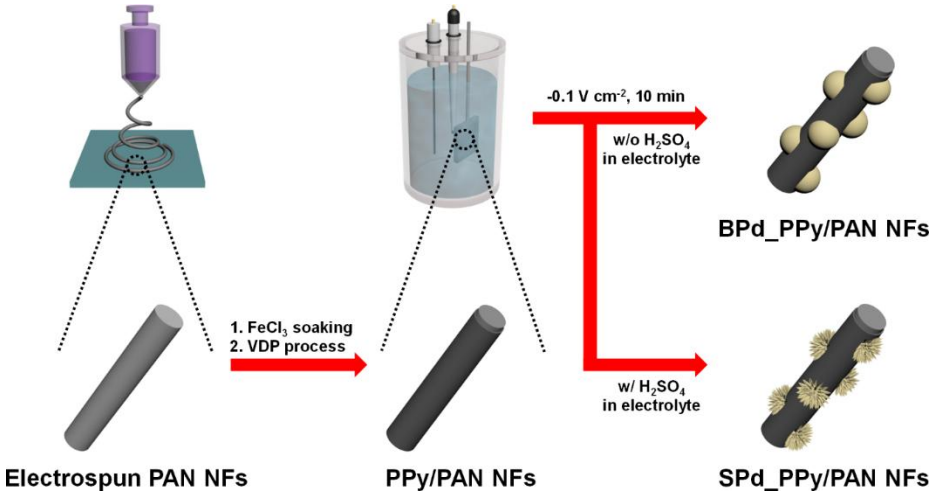

Figure 11. Illustrative diagram of the sequential fabrication procedure for shape-controlled Pd NPs-decorated PPy/PAN NFs using an electerospinning, vapor deposition polymerization and three-electrode system-based electrodeposition with (w/) or without (w/o) H_2SO_4 in electrolyte.

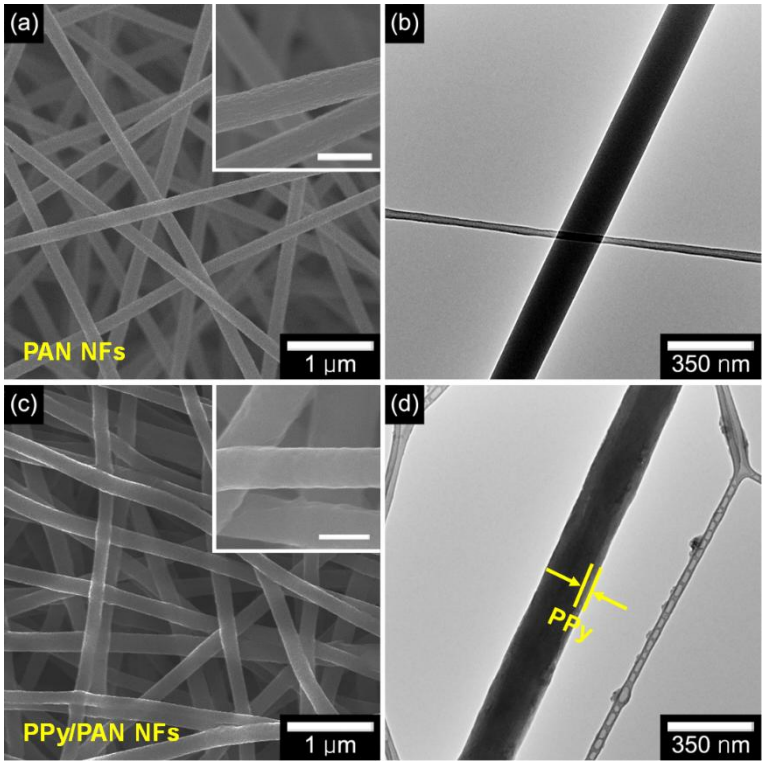

Figure 12. Low- and high-magnification (inset) FE-SEM and TEM images of (a,b) PAN NFs and (c.d) PPy/PAN NFs (scale bae of inset: 200 nm).

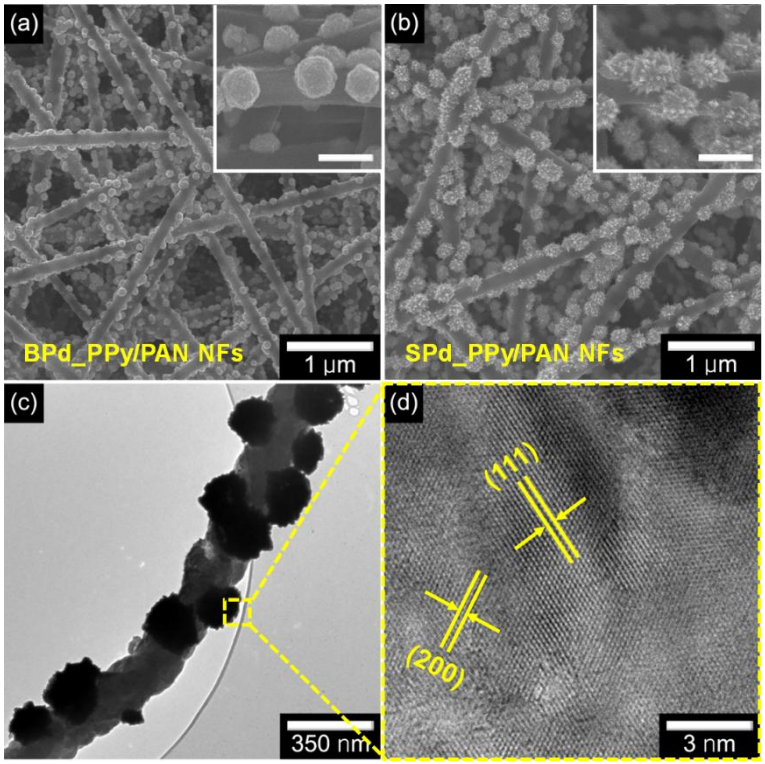

Figure 13. FE-SEM images of (a) BPd_PPy/PAN NFs and (b) SPd_PPy/PAN NFs. (c) TEM and (d) HR-TEM images of SPd_PPy/PAN NFs.

3.1.2 Characterization of shape-controlled Pd_PPy/PAN NFs

The powder X-Ray Diffraction (XRD) patterns provide additional information about the structure development at the each fabrication steps (**Figure 14**). Electrospun PAN NFs shows a characteristic diffraction peak at 2θ angle of 16.8°, indicating the the orthorhombic (110) reflection. These strong peak was also discovered for other sample, which indicates that the PAN structure was maintained during the VDP and electrodeposition. However, the broad peak at 23° was enhanced due to the amorphous PPy structure which is derived from scattering by the PPy chains at the interplanar spacing. The diffraction peaks at 2θ = 40. 12 for (111), 46.3 for (200), 67.8 for (220) and 81.6 for (311) is well-matched with fcc lattice of Pd, indicated that Pd is successfully reduced by fed electrons in electrodeposition process. **Figure 15** shows the RAMAN spectrum over the range from 1000 to 2000 cm^{-1}. The D band is assigned to typically representative of disordered graphite, and G band attributed to in-plane displacement of carbon atoms in aromatic structure. Therefore, the I_D/I_G ratio (ratio of intensity the D and G bands) is facilitates the determination of the degree of graphitization. While no features appear in electrospun PAN NFs, two characteristic peak is observed due to the coated PPy. The

I_D/I_G ratio of the SPd_PPy/PAN NFs is higher than the PPy/PAN NFs, implying that the decoration of Pd within the PPy decreased the degree of graphitization. The chemical composition is investigated using X-ray Photoelectron Spectroscopy (XPS). **Figure 16a** presents fully spectrum over the range 0 - 1200 eV, indicating that Pd was formed in SPd_PPy/PAN NFs. Furthermore, High-resolution XPS spectra for the Pd region are displayed in **Figure 16b**. Spin-orbit component $3d_{5/2}$ and $3d_{3/2}$ are observed near 335 and 341 eV, illustrating that the valence state of Pd was zero.

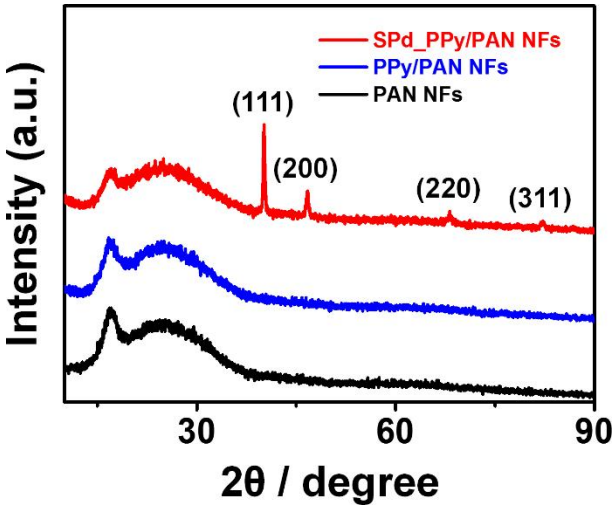

Figure 14. XRD spectrum for PAN NFs (black), PPy/PAN NFs (blue) and SPd_PPy/PAN NFs (red), respectively.

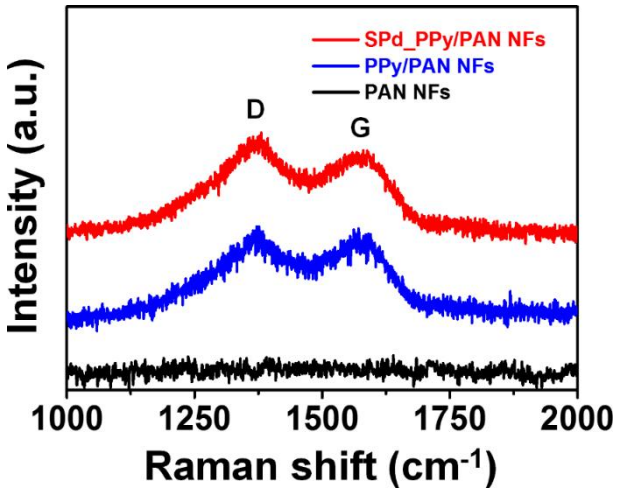

Figure 15. RAMAN spectra for PAN NFs (black), PPy/PAN NFs (blue) and SPd_PPy/PAN NFs (red), respectively.

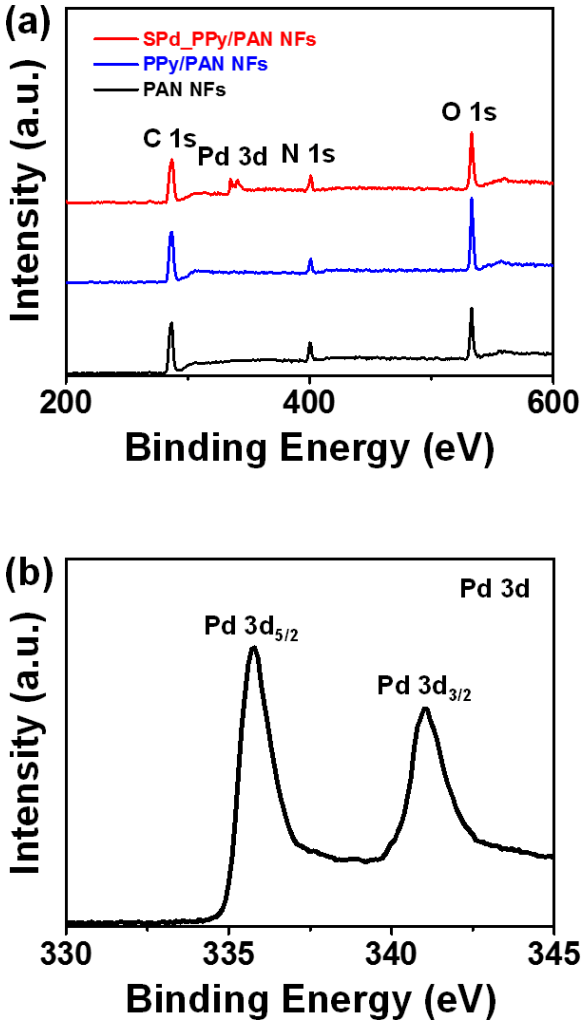

Figure 16. (a) XPS of fully scanned spectrum for PAN NFs (black), PPy/PAN NFs (blue) and SPd_PPy/PAN NFs (red). (b) High-resolution XPS of Pd 3d for SPd_PPy/PAN NFs.

3.1.3 Electrical properties of shape-controlled Pd_PPy/PAN NFs electrode

The current-voltage (*I-V*) plots of PPy/PAN NFs and Pd_PPy/PAN NFs with different shape are measured by top-gate voltage (V_G)-contact. The *I-V* plot is investigated by the intrinsic electric property (**Figure 17a**). All fabricated samples displayed linear *I-V* curves in the voltage range to -0.1 from +0.1 V, indicating ohmic contact. It can be concluded that the Pd_PPy/PAN NFs based electrode make dependable electrical contact for ultrasensitive biosensors. Furthermore, the conductivity (*dI/dV*) of Pd_PPy/PAN NFs is increased by comparison with PPy/PAN NFs, due to the improvement by metal (Pd). **Figure 17b** presensts the I_{SD}-V_{SD} curves of Pd_PPy/PAN NFs with a regular interval V_G in steps of -0.1 V at a constant scan rate (10 mV s^{-1}). According to the decrease of V_G, the I_{SD} is also decreased; this is due to the p-type behavior (major carrier: hole) of PPy as charge transfer channel in FET-type system.

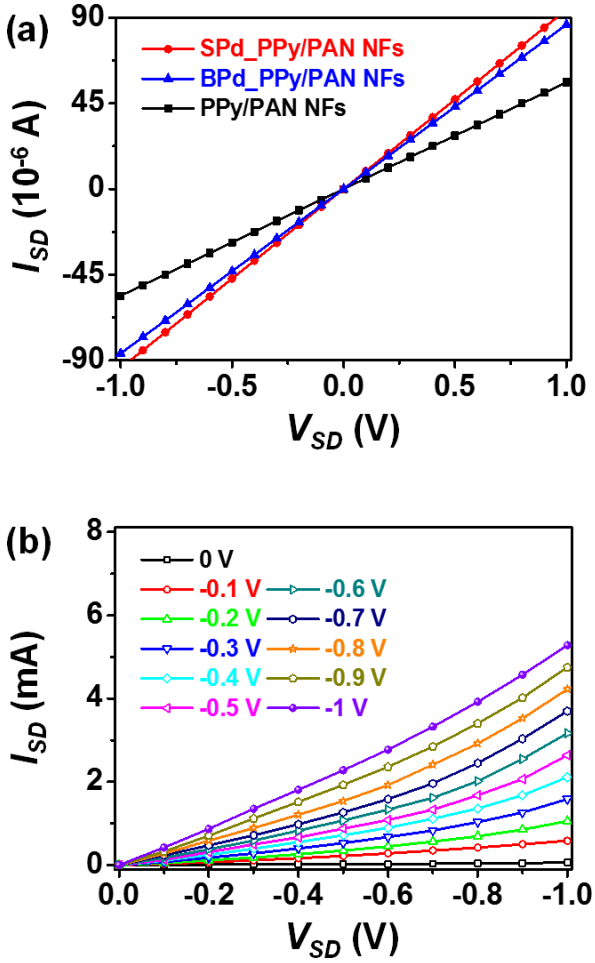

Figure 17. (a) Source-drain current versus source-drain voltage (I_{SD}-V_{SD}) curves of PPy NFs (black), BPd_PPy/PAN NFs (blue) and SPd_PPy/PAN NFs (red), respectively. (b) I_{SD}-V_{SD} output characteristic of SPd_PPy/PAN NFs based liquid-ion-gated FET-type sensor with different gate voltage (V_G) from 0 to -1 V in step of -0.1 V (scan rate of V_{SD}: 10 mV s^{-1}).

3.1.4 Real-time response of FET-type H_2O_2 sensor based on shape-controlled Pd_PPy/PAN NFs electrode

The I_{SD} is measured at a V_G of -100 mV (V_{SD} = 1 mV) to investigate the sensing properties of the liquid-ion-gated shape-controlled Pd_PPy/PAN NFs based FET-type electrode which consists of source (*S*), drain (*D*) and gate voltage. As shown in **Figure 18**, the sensing mechanism of the Pd_PPy/PAN NFs is described as follows: added H_2O_2 was oxdized with two electron by catalytic effect of Pd. These two electrons transfer to the top-gate voltage, which became more negative. Consequently, the density of the carrier (hole) in the charge transfer pathway of PPy/PAN NFs is increased, leading to the current increase. Moreover, H_2O_2 also improves the oxidation level ($[N^+]/[N]$ ratio), inducing an increased number of holes in the PPy backbone and current increase as before.

To investigate the sensing properties of the liquid-ion-gated SPd_PPy/PAN NFs based FET-type sensor, the I_{SD} was monitored in real time at a V_G of -0.1 V (V_{SD} = 1 mV), a low operating voltage, according to the addition of various concentration of H_2O_2. **Figure 19a** represents the real-time response of the PPy/PAN NFs, BPd_PPy/PAN NFs, and SPd_PPy/PAN NFs as a function of H_2O_2

concentration. When the H_2O_2 added, the I_{SD} was rapidly decreased within 1 s before reaching its saturated value. Although the detection limit of PPy/PAN NFs is very low (1 mM), the current is increased by increasing the hole density due to the direct oxidation of the PPy, which is explained above (**Figure 20**). On the other hand, the sensitivity of the SPd_PPy/PAN NFs is higher than BPd_PPy/PAN NFs illustrating that more pointed Pd nanoparticles provides the more active site, which has enhanced catalytic effect toward H_2O_2; that is, the SPd_PPy/PAN NFs was capable of detecting H_2O_2 concentration as low as 1 nm at room temperature. **Figure 19b** presents the sensitivity change as a function of concentration of H_2O_2. The sensitivity (S) was defined from the saturation point of the normailized current change ($(\Delta I/I_0)_{SD}$ x 100), measured 10 s after addition of H_2O_2. At low concentration (<100 nM), the Pd_PPy/PAN NFs based FET-type sensors showed nonlinear changes. Contrastively, linear behavior was observed over a wide concentration range (10^0 – 10^4 nm).

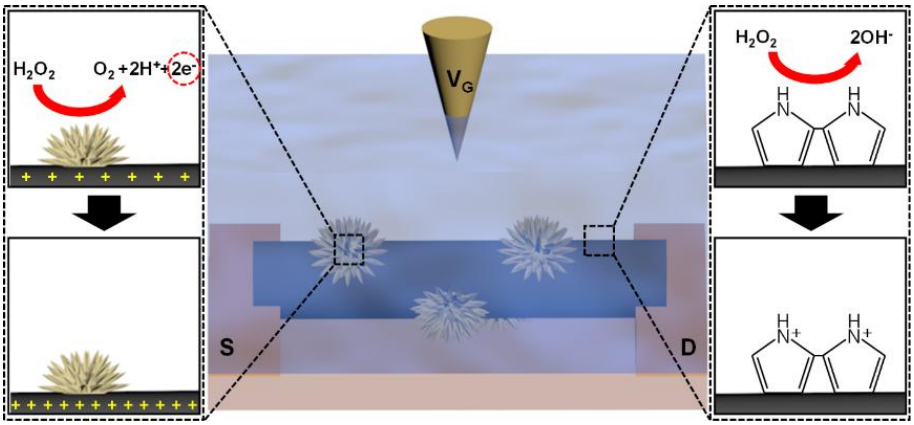

Figure 18. H_2O_2 detection mechanism of SPd_PPy/PAN NFs on the SPd surface (left) and PPy surface (right).

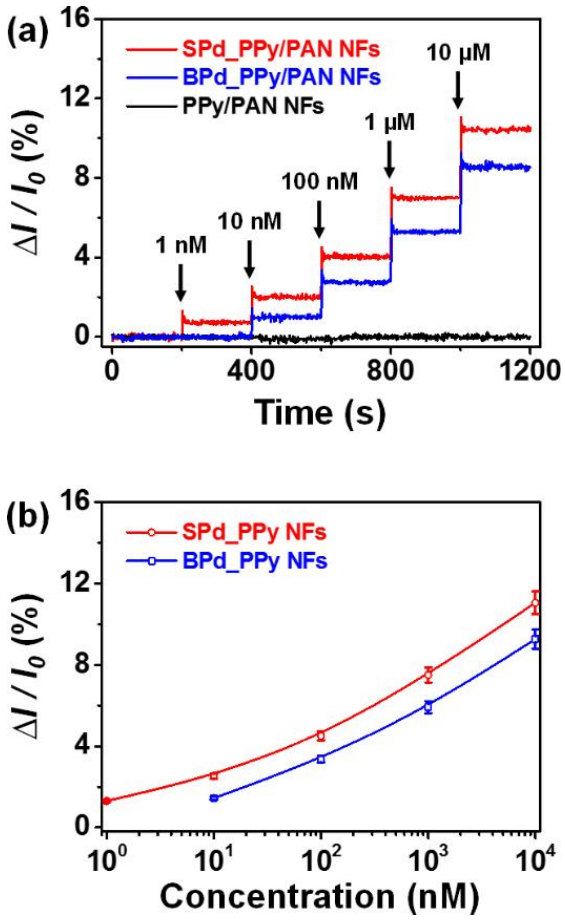

Figure 19. (a) Real-time response for the FET-type sensor with normalized current changes ($\Delta I/I_0 = (I-I_0)/I_0$, where I_0 is the initial and I is the immediate current). (b) Calibration curves of current changes as a function of glucose concentration (PPy/PAN NFs (black); BPd_PPy/PAN NFs (blue); SPd_PPy/PAN NFs (red)).

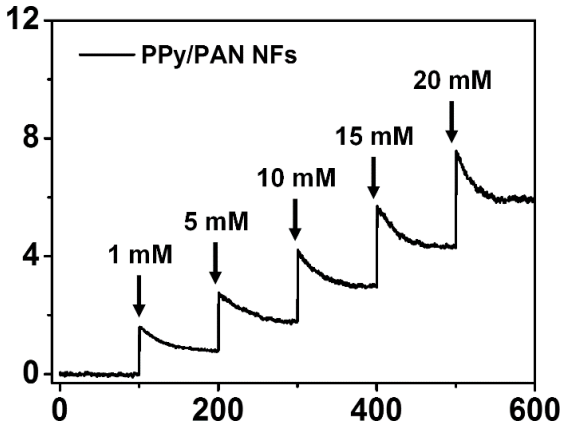

Figure 20. Real-time response for the PPy/PAN NFs-based FET-type sensor with normalized current changes.

3.2 Fabrication of population-controlled flower-like NCs-decorated CVD graphene electrode for ultrasensitive and flexible hydrogen gas sensing

3.2.1 Fabrication of population-controlled FPNCs_CG

Figure 21 illustrates the overall procedure for the fabrication of flower-like palladium (FPNCs) decorated CVD graphene (CG) electrodes. CG is grown on copper (Cu) foil using methane (CH_4) as carbon source and hydrogen (H_2) as a catalyst [119,120]. The Cu foil is removed with a Cu-etchant and the CG is transferred to a poly(ethylene naphthalene) (PEN) substrate for flexibility. Before the electrodeposition, the surface of the CG is chemically functionalized with amino groups by reacting with 1,5-diaminonaphthalene (DAN), which orients into flat stacks on the graphene surface due to π-π interactions between the phenyl group of DAN and aromatic structure of the graphene. To confirm the chemical functionalization of the CG surface, RAMAN spectra of DAN-treated and -untreated CG surface are shown in **Figure 22a**. The D peak (1354 cm^{-1}) generates after the DAN treatment, owing to the disorder of the graphene basal plane. Furthermore, The I_{2D}/I_G intensity ratio of surfaces that is untreated with DAN (*ca.* 3.7) is higher than that of DAN-treated surfaces (*ca.*

1.8). This change suggested that charge impurity or rippling on the surface cause an inhomogeneous charge distribution and electron-donating containing aromatic molecules induced a ratio decrease due to the doping effect. Additionally, the upshift of 2D and downshift of G band wavenumber can be observed by electrical gating, owing to the dynamic effect of carrier population [121,122]. Then, Pd is directly deposited onto the DAN-treated and -untreated graphene surface as working electrode with a Pd precursor contained sulfuric acid electrolyte in a three-electrode system. In case of DAN-untreated graphene, Pd^{2+} ions react with numerous functional group on the graphene surface induced by moisture, oxygen, and fabrication process, resulted in evenly spread hexagonal pyramid structure as exhibited in **Figure 23** [123]. Conversely, partial negative charges on the nitrogen atoms of DAN preferentially combine with Pd^{2+} ions than the other functional groups. Pd nanoparticles (NPs) are then deposited on the graphene surface. With increasing electrodeposition time, flower-like palladium nanoclusters (FPNCs) are formed from these Pd NPs as nucleation sites (**Figrue 24**). FPNCs formation mechanism can be explained as following reason [117,118]. Sulfate ions (SO_4^{2-}) in sulfuric acid theoretically prohibit the growth of Pd at the adsorption

sites. Furthermore, this effect is maximized on the Pd (111) plane, which is preferred adsorption plane for SO_4^{2-} ions. To confirm the influence of sulfate ions, sulfuric acid as electrolyte is prepared with various concentration (0.01 and 0.1 M) as shown in **Figure 25**. Smooth structure is observed at high concentration of H_2SO_4, due to the uniformly hindrance of the growth of (111) plane on the Pd surface. Adversely, low concentration induce to the partial hindrance, resulted in more sharp structure. This result indicate that Pd is predominantly composed of (111) plane and the growth of Pd can be controlled by sulfate ions concentration. FE-SEM micrographs of FPNC_CG surfaces with various populations of FPNCs are shown in **Figure 26a–c**. The population of FPNCs increase with increasing DAN concentration from 0.01 to 0.1 M, suggesting that the degree of modification is proportional to the number of Pd NPs as nuclei. In addition, the FPNCs are approximately *ca.* 300 nm in size and compose of numerous needles of hexagonal pyramids (**Figure 26d**) with *ca.* 80 nm in length (**Figure 26e**). The HR-TEM images in **Figure 26f** shows that the FPNCs are highly crystallized, as indicated by well-defined fringe patterns. The corresponding FFT diffractogram shows a six-fold symmetry of diffraction spots indicative of hexagonal

faces bound by the (111) plane, as described above. In addition, the interplanar spacing calculated from the FFT analysis of the micrograph is *ca.* 0.22 nm, which is consistent with the atomic spacing of (111) face-centered-cubic (fcc) Pd [124-129]. The FPNCs deposited on CG with functionalization solutions containing 0.01, 0.1, and 1 M DAN are denoted FPNCs_CG_L, FPNCs_CG_M, and FPNCs_CG_H, respectively.

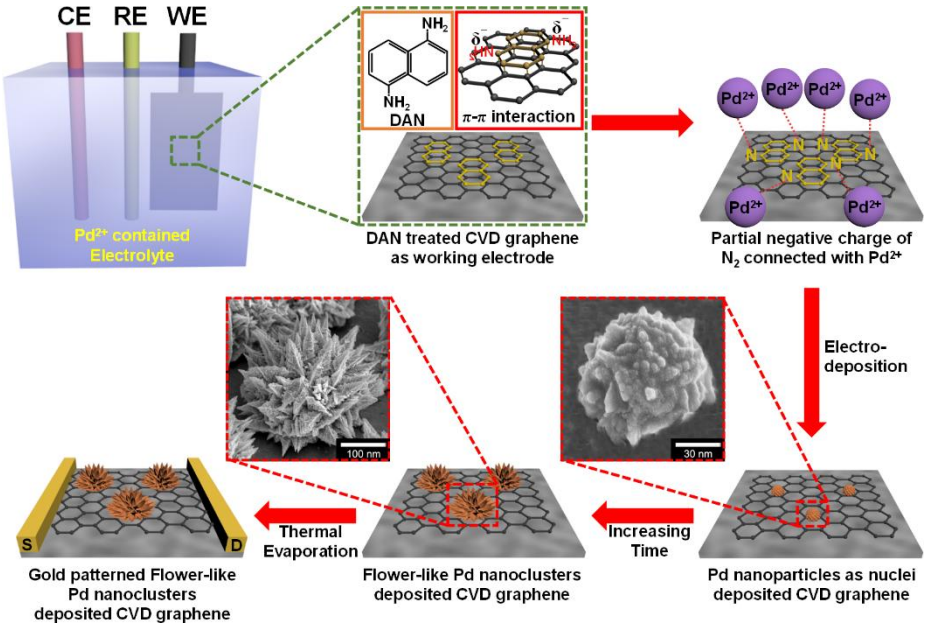

Figure 21. Illustrative diagram for the fabrication steps of FPNCs_CG electrode.

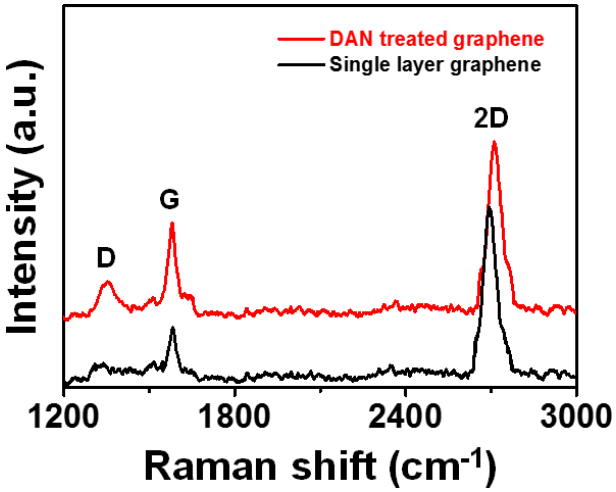

Figure 22. RAMAN of singler layer graphene untreated (black) and treated (red) with DAN.

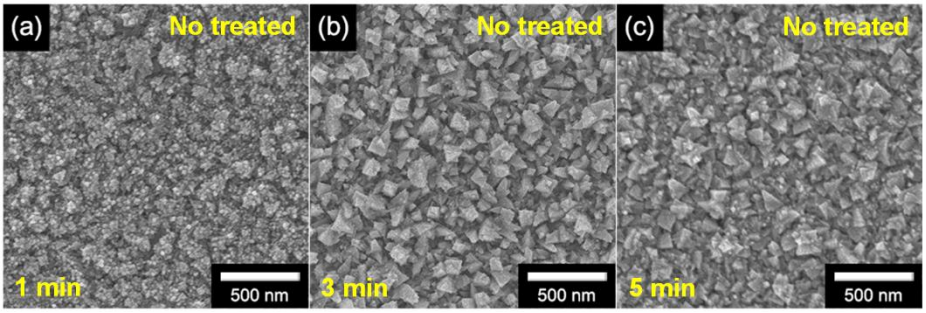

Figure 23. FE-SEM images of FPNCs_CG untreated with DAN for (a) 1 min, (b) 3 min, and (c) 5 min, respectively.

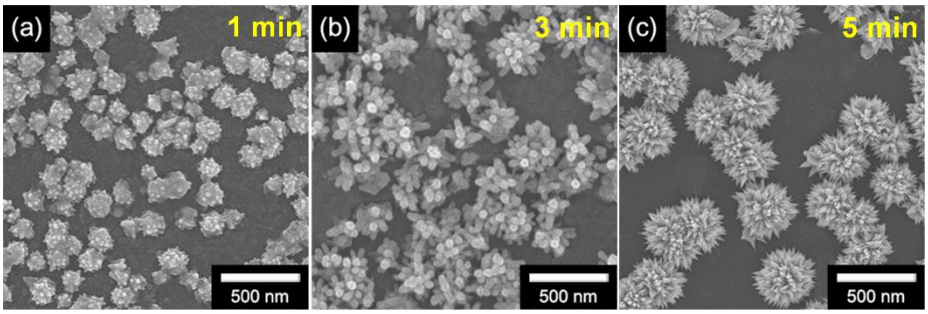

Figure 24. FE-SEM images of FPNCs_CG treated with DAN for (a) 1 min, (b) 3 min, and (c) 5 min, respectively.

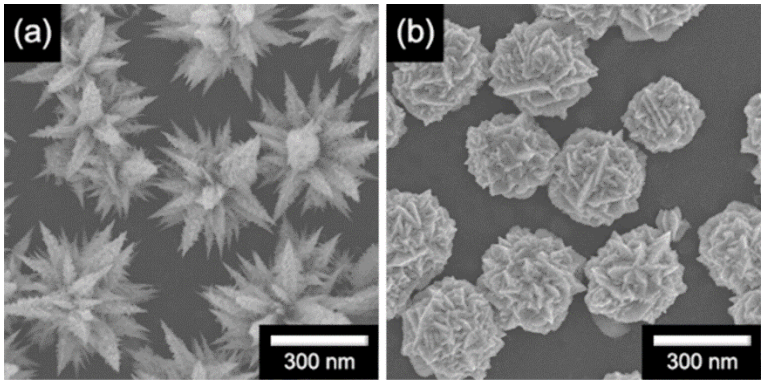

Figure 25. FE-SEM images of FPNCs_CG using sulfuric acid of (a) 0.01 M and 0.1 M as electrolyte.

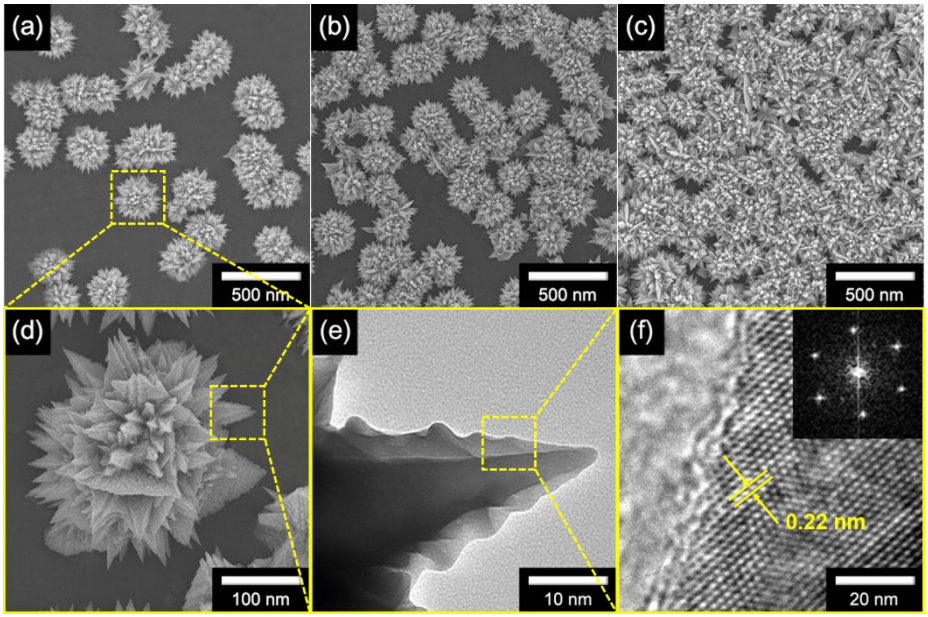

Figure 26. FE-SEM images of FPNCs_CG with various population of FPNCs ((a) low, (b) medium, and (c) high). (d) High-resolution SEM, (e) TEM images, (f) HR-TEM and FFT pattern (inset) of FPNCs_CG.

3.2.2 Characterization of population-controlled FPNCs_CG

Energy Dispersive X-ray (EDX) spectra revealed that the FPNCs are composed of Pd and carbon elements, implying that the FPNCs are deposited on the graphene surface (**Figure 27**). The chemical composition of FPNCs_CG films is investigated by X-ray Photoelectron Spectroscopy (XPS). **Figure 28a** displays the full spectra acquired from 0 to 1000 eV. Only C, O, and Pd are present. The Pd 3d peak can be accurately fit with two prominent peaks at 335 and 341 eV, indicating that the Pd^{2+} ions are completely reduced to Pd^{0} during the electrodeposition process (**Figure 28b**).

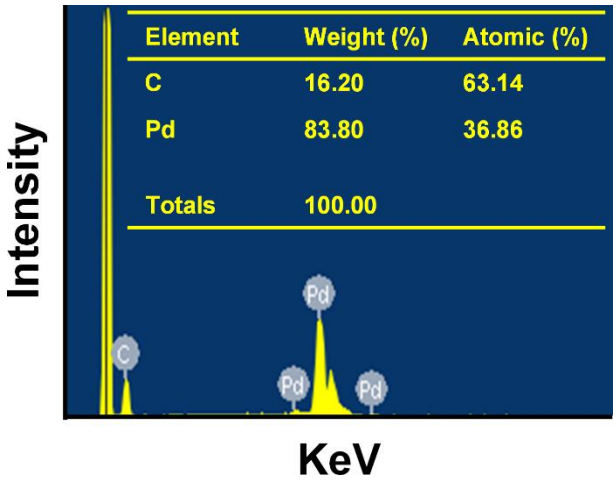

Figure 27. EDX spectra of FPNCs_CG.

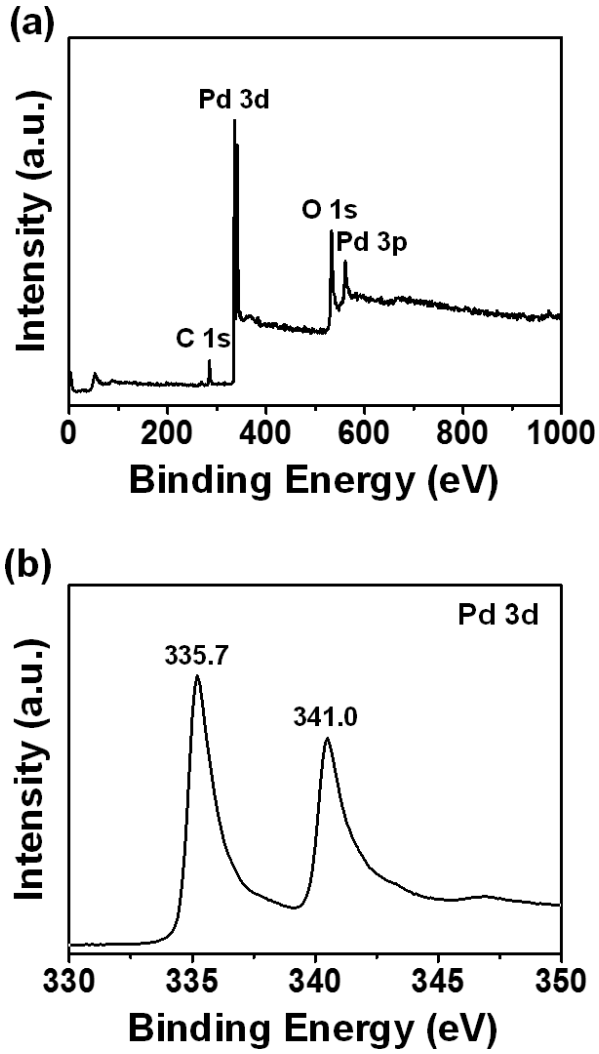

Figure 28. (a) Fully spectrum and (b) Pd 3d spectrum of FPNCs_CG.

3.2.3 Electrical properties of population-controlled FPNCs_CG electrode

Figure 29a–d show FE-SEM micrographs of gold deposited FPNCs_CG electrode with various populations of FPNCs, demonstrating that the population of FPNCs can be well controlled. **Figure 30** shows current-voltage (*I–V*) curves of the FPNCs_CG films and indicates that the FPNCs are in ohmic contact with graphene surface. Contact resistance increases slightly with increasing of the FPNCs population, implying that the FPNCs acts as impurity for decrease of quality. However, this slight change in contact resistance may be ignored in practical applications due to the overall high conductivity of the FPNCs_CG films.

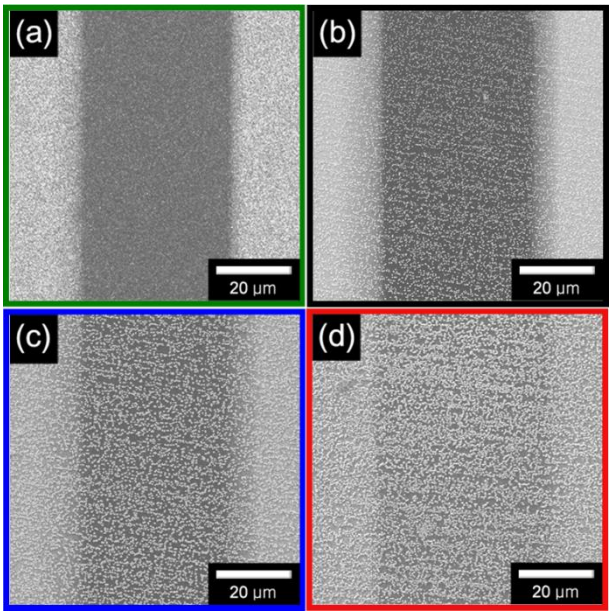

Figure 29. FE-SEM images of (a) pristine CG, (b) FPNCs_CG_L, (c) FPNCs_CG_M, and (d) FPNCs_CG_H, respectively.

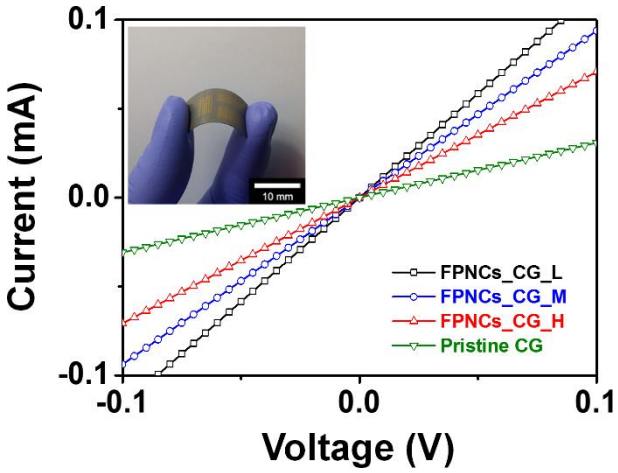

Figure 30. Real-images of flexible electrode deposited with the gold pattern (inset) and *I-V* curves of CG (green), FPNCs_CG_L (black), FPNCs_CG_M (blue), and FPNCs_CG_H (red), respectively.

3.2.4 Real-time response of chemiresistive H_2 sensor based on population-controlled FPNCs_CG electrode

Figure 31 shows the real-time response of a FPNCs_CG electrode to an H_2 atmosphere at room temperature. The resistance change, ΔR, of the electrode is monitored during sequential or periodic exposures to H_2. $\Delta R/R_0$ (sensitivity) is defined as the percent resistance change upon exposure to a gas with a fixed concentration of hydrogen and is calculated as follows:

$$\frac{\Delta R}{R_0} = \frac{(R - R_0)}{R_0}$$

,where R_0 is the resistance of the sensor exposed to dry air and R is the maximum resistance after exposure to a gas containing hydrogen. When the FPNCs_CG is exposed to hydrogen gas, the phase of the FPNCs is transfered from palladium (Pd) to palladium hydride (PdHx). Consequently, decreasing of the work function is beneficial to the flow of more electrons, resulted in decreasing of the resistance as represented in **Figure 32** [130-132]. Resistance of the films is measured in real time upon exposure to various concentrations of H_2 gas. In contrast to pristine CG, all of the FPNCs_CG sensors exhibit a rapid and reversible response to H_2 gas at room temperature. **Figure 31a** shows the electode response during sequential exposures

of increasing analyte concentration (0.1, 1, 10, 50, and 100 ppm). Sensitivity increases with increasing populations of FPNCs, indicating that the population of FPNCs is active materials to react with hydrogen atoms. The minimum detectable level (MDL) of H_2 measured with the FPNCs_CG_H (0.1 ppm) is lower than that of FPNCs_CG_L (10 ppm). This is likely because higher populations of FPNCs provide more reactive sites for hydrogen atoms. Furthermore, the detection limit of FPNCs_CG_H is three orders of magnitude lower than that of noble metal/graphene based electrodes (**Table 1**). The electrical response of a FPNCs_CG electrode upon periodic exposures to 10 ppm H_2 is shown in **Figure 31b**. Testing over five cycle yields similar responses and sensitivity without abatement. Furthermore, the sensitivity is directly proportional to the square root of H_2 concentration as shown in **Figure 31c**. This can be explained by the Langmuir adsorption isotherm theory about dissociates of hydrogen molecule upon adsorption on the Pd surface [126,133]. The H_2 dissociation reaction on Pd surface can be describes as

$H_2 + 2Pd \leftrightarrow 2PdHx$

The adsorption and desorption rate of hydrogen are $k_1 p\,(1-\theta)^2$ and $k_{-1}\theta^2$ (where, k_1 and k_{-1} are the adsorption and desorption

constant, respectively). p is partial pressure of H_2, and θ is the fraction of Pd covered by hydrogen that is proportionate to sensitivity$\Delta R/R_0$. The adsorption rate equals the desorption rate at equilibrium,

$k_1 p\,(1-\theta)^2 = k_{-1}\theta^2$ or $\theta/(1-\theta) = (k_1/k_{-1})^{1/2}p^{1/2}$

At low concentration of H_2 (θ << 1), the sensitivity is proportional to the square root of the partial pressure and concentration of H_2 as follows:

$$\Delta R/R_0 \propto \theta \approx (k_1/k_{-1})^{1/2}p^{1/2}$$

The response time (τ) as a function of hydrogen concentration is exhibited in **Figure 31d**. The response time is increased with increasing population of FPNCs, indicated that large active sites are required more time to saturate. Furthermore, reciprocal of the response time 1/τ follows a linear correlation with hydrogen concentration. The adsorption rate of H_2 is $\mathrm{r} = k_1 p(1-\theta)^2$, and θ is negligible at the low concentration. Therefore, the adsorption rate is estimated to ber $= k_1 p = k_1[\mathrm{H_2}]$, which is well-matched in inset of **Figure 31d**.

The electrodes were operated in dry air (using only N_2 flow; humidity: at below *ca.* 10 %), however, the humidity was important factor for sensitivity and response/recovery time. The sensing performance was

measured at wet air (using bubbled water with N_2 flow; humidity: *ca.* 30 %) to investigate the effect of humidity. The resistance of FPNCs_CG electrodes decreased at both water drop and bubbled water, implying that water obviously influenced the resistance (**Figure 33a and b**). When the exposed to hydrogen gas with wet air, the strong peak and fast response/recovery time could be confirmed compared to drying condition (**Figure 34**). This is because functional groups related to oxygen on the graphene surface is preferentially adsorbed with water vapor and decreases the p-type doping, resulted in decrease of the resistance [134-136]. The FPNCs_CG based sensors also exhibited high selectivity for H_2 gas compared to nitrogen dioxide (NO_2) and ammonia (NH_3) gas (**Figure 35**). When the pristine CG was exposed to NO_2 gas, the resistance decreased (**Figure 35a**). On the other hands, the resistance upon exposure to NH_3 gas shows increasing tendency (**Figure 35b**). This is because NO_2 and NH_3 gases is electron acceptors and electron donor gas, resulted in change the hole concentration of graphene (p-type) [137-140]. According to the deposition of FPNCs, the resistance toward both gases increased, due to the reduced carrier mobility by the scattering effect of Pd. Furthermore, Sensitivity and MDL of NO_2 and NH_3 were lower than

that of hydrogen gas, due to the different sensing mechanism of hydrogen (phase transition), indicating that FPNCs_CG based sensor show the high selectivity [141].

The resistance of the FPNCs_CG electrode depended on the bend radius of the film-substrate assembly. Therefore, the resistance of the FPNCs_CG as a function of bend radius, shown in **Figure 36a**, is used to evaluate the mechanical stability of FPNCs_CG sensors on PEN substrates [134,142-144]. No significant change in resistance is observed down to a bend radius of *ca.* 10 mm. **Figure 36b** shows the change in sensor response after repeated bending and relaxing. The response decreases by only 2 % after 100 bending cycles. Furthermore, the morphology of the FPNCs is maintained without collapse even after 100 cycles of H_2 exposure (**Figure 37 a and b**). This demonstrates the excellent mechanical flexibility and durability of the FPNCs_CG sensor electodes and shows that these film may be useful in wearable sensors [145-148].

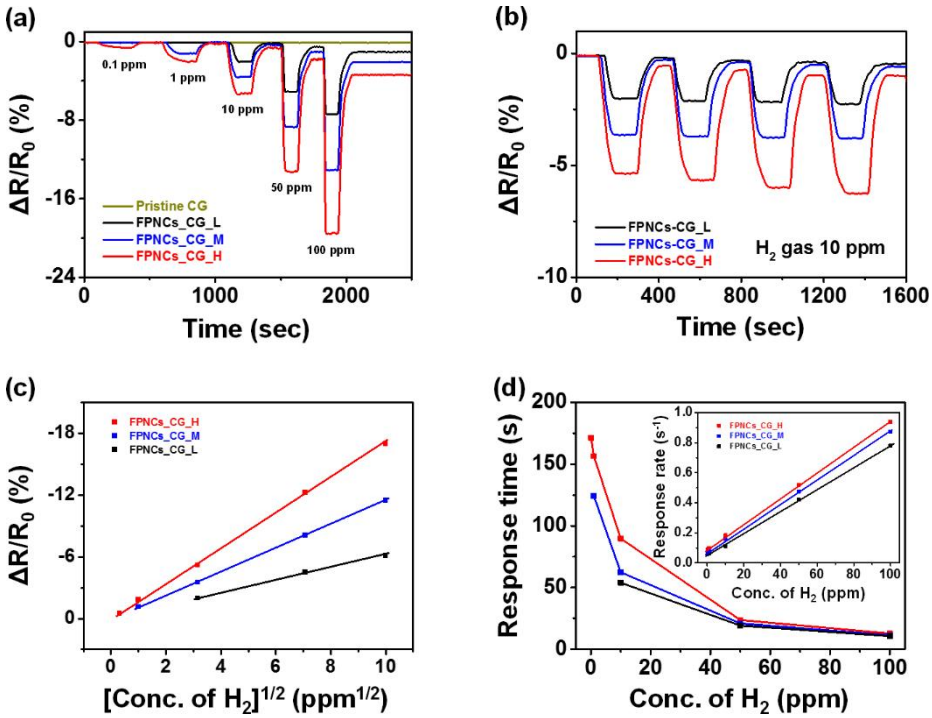

Figure 31. Reversible and reproducible responses are measured with various populations of FPNCs_CG at a constant current value (10^{-4} A). Nomalized resistance changes at room temperature upon (a) sequential exposure to H_2 gas of various concentrations (0.1 to 100 ppm) and (b) periodic exposure to H_2 gas (10 ppm) of Pristine CG (green), FPNCs_CG_L (black), FPNCs_CG_M (blue), and FPNCs_CG_H (red), respectively. (c) Sensitivity as a function of square root of H_2 concentration, (d) response time and rate (inset) as a variation of H_2 concentration.

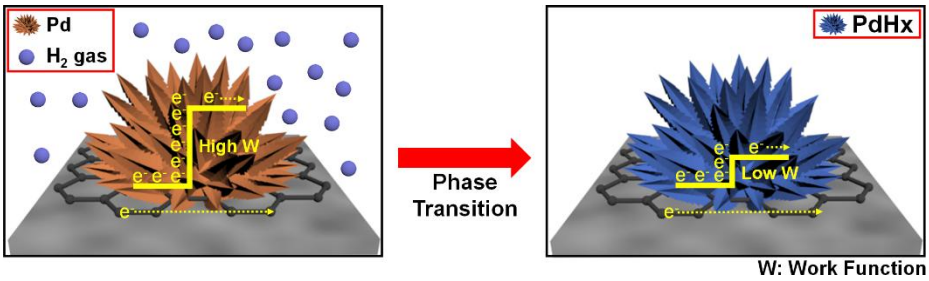

Figure 32. Scheme of hydrogen gas sensing mechanism of F P N C s _ C G .

Table 1. Hydrogen sensing performance of this work compared with the literature.

Sensing materials	MDL[a)]	Reference
FPNCs_CG	0.1 ppm	This work
Pd NPs/Graphene nanoribbon	40 ppm	139
Pd/rGO	1 %	144
Pd NPs/CVD[b)] graphene	1000 ppm	141
Pd-doped reduced graphene oxide	200 ppm	142

a) MDL, minimum detectable level; b) CVD, chemical vapor deposition.

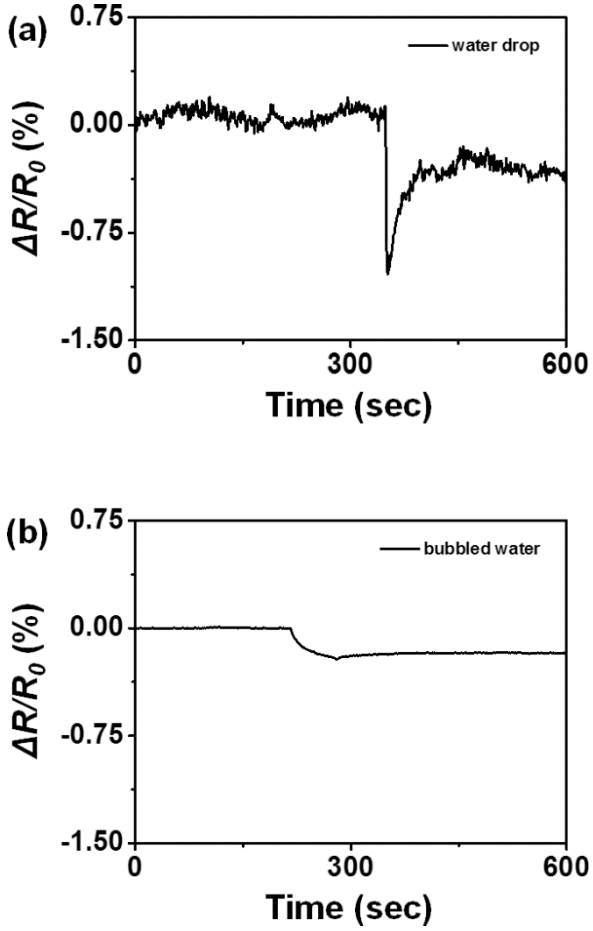

Figure 33. Reversible and reproducible responses are measured with FPNCs_CG_H at a constant current value (10^{-4} A). Nomalized resistance changes at room temperature upon exposure to H_2 gas with (a) water drop and (b) bubbled water.

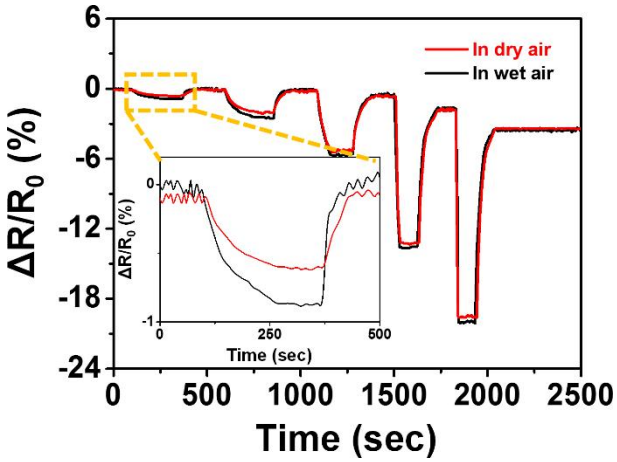

Figure 34. Reversible and reproducible responses are measured with FPNCs_CG_H at a constant current value (10^{-4} A). Nomalized resistance changes at room temperature with sequential exposure to H_2 gas of various concentration (0.1 to 100 ppm) in dry (red) and wet (black) air.

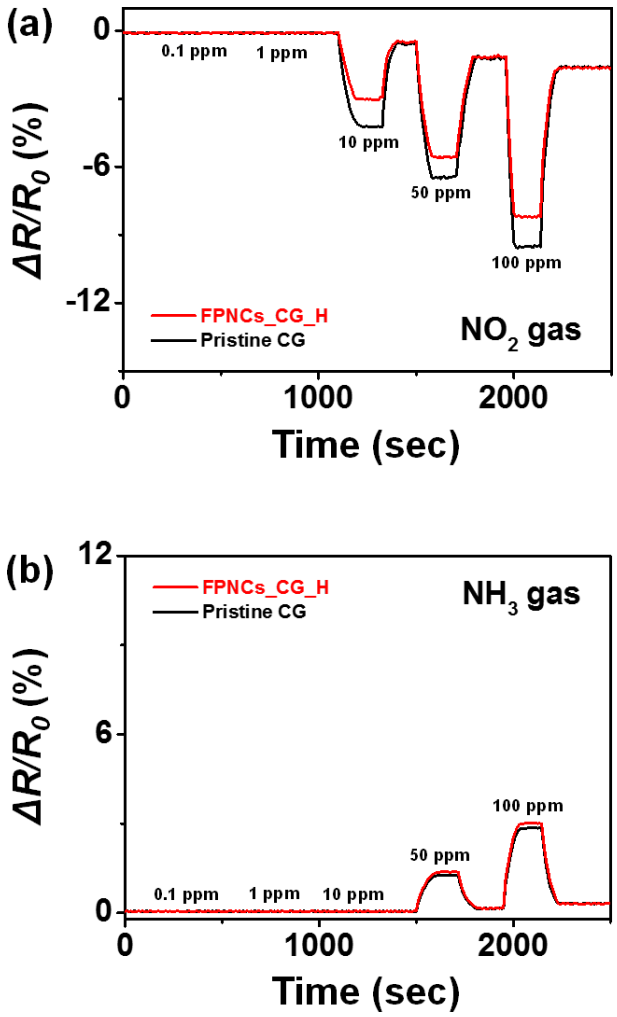

Figure 35. Reversible and reproducible responses are measured at a constant current value (10^{-4} A). Nomalized resistance changes at room temperature upon sequential exposure to (a) NO_2 and (b) NH_3 gas of various concentration (0.1 to 100 ppm) with Pristine CG (black) and FPNCs_CG_H (red), respectively.

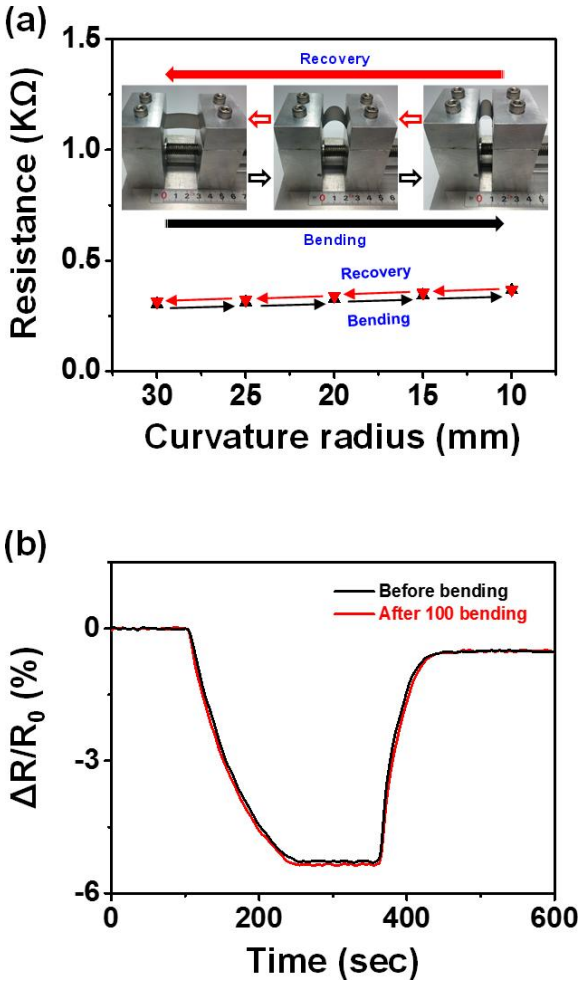

Figure 36. (**a**) Resistance changes of flexible H_2 sensor electrode for different curvature radius, and (**b**) Sensing behavior of the H_2 gas (10 ppm) before and after 100 bending of FPNCs_CG_H. FE-SEM images of FPNCs_CG.

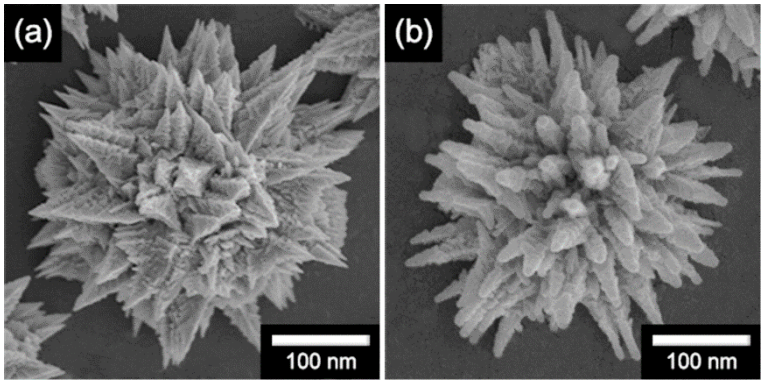

Figure 37. FE-SEM images of FPNCs_CG (a) before and (b) after H_2 gas sensing for 100 cycles.

3.3 Fabrication of sharpness controlled Pd nanoflower-decorated CVD graphene electrode for selectivity-improved FET-type glucose sensor

3.3.1 Fabrication of sharpness-controlled PNFG

Shape-controlled palladium nanoflower-decorated CVD graphene (SPNFG) was fabricated *via* surface functionalization and electrodeposition method. Prior to the electrodeposition process, single layer graphene was grown on copper (Cu) foil by chemical vapor deposition (CVD) in a vacuum chamber with CH_4 as the carbon source and H_2 as the carrier gas at 1000 °C. Then, the Cu was eliminated using an etchant solution and the floating graphene was transferred onto the substrate [149,150]. The CVD graphene was immersed in a methanolic solution of 1,5-diaminonaphthalene (1 M, DAN) to chemically functionalize with amino groups. The DAN molecule lays flat on the graphene surface owing to π-π interactions between the aromatic structure of graphene and the phenyl groups of DAN. When a constant voltage was applied using a three-electrode system, palladium ion (Pd^{2+}) was reduced to palladium (Pd^0) by the electron supplied from the graphene surface. Despite numerous oxygen-containing functional groups on the graphene surface, the amino groups of DAN

preferentially interacts with palladium ion, resulted in formation of the Pd^0 as a nucleation site. Pd was then grown from the nucleation site to the nanoflower structure that was affected by the hindering effect of sulfate ions in the electrolyte [151,152]. Field Emission-Scanning Electron Microscope (FE-SEM) images of the SPNFG are suggested in **Figure 38**. Uniform decoration of PNF on the entire graphene surface was evident at all magnifications, which indicated that the high concentration of DAN led to wide spread nucleation. Furthermore, **Figure 38 (c, f and i)** reveals that the size of the PNFs was unchanged despite the various concentration of sulfuric acid in the electrolyte. The shape was investigated as a function of the sulfuric acid concentration (0.01, 0.1 and 1 M) in electrolyte; adjusting the DAN concentration provided discrete PNF. At the highest sulfuric acid concentration, the PNF was grown as a blunt shapes on account of overall growth inhibition (**Figure 38c**). On the other hand, the pointed PNF was formed by partially disturbance at the low concentration (**Figure 38i**). This results make it clear that the sharpness of PNFs is increased with decreasing concentration of sulfate ions in the electrolyte. The SPNFG synthesized with electrolyte solutions containing sulfuric acid at 0.01, 0.1, and 1M were denoted as SPNFG_L, SPNFG_M, and SPNFG_H,

respectively.

Figure 39a represents High Resolution-Transmission Electron Microscope (HR-TEM) micrographs of the CVD graphene; it was clearly single-layer graphene. RAMAN spectroscopy is a useful analytical tool to examine single-layer graphene. The ratio of the G (*ca.* 1587 cm^{-1}) to 2D (*ca.* 2697 cm^{-1}) implies the number of graphene layers. The CVD graphene examined here had an I_{2D}/I_G ratio of *ca.* 1.82, which indicated the single layer graphene (**inset of Figure 39a**). The TEM images of PNFs in **Figure 39b and d** exhibit that the PNF is *ca.* 300 nm and consisted of numerous rods of having hexagonal pyramid shape (*ca.* 100 nm in length). Additionally, HR-TEM images of the PNFs reveal interplanar spacing of 0.195 nm for the (200) and 0.224 nm for the (111) planes, which correspond to face-centered-cubic (fcc) Pd (**Figure 39c**).

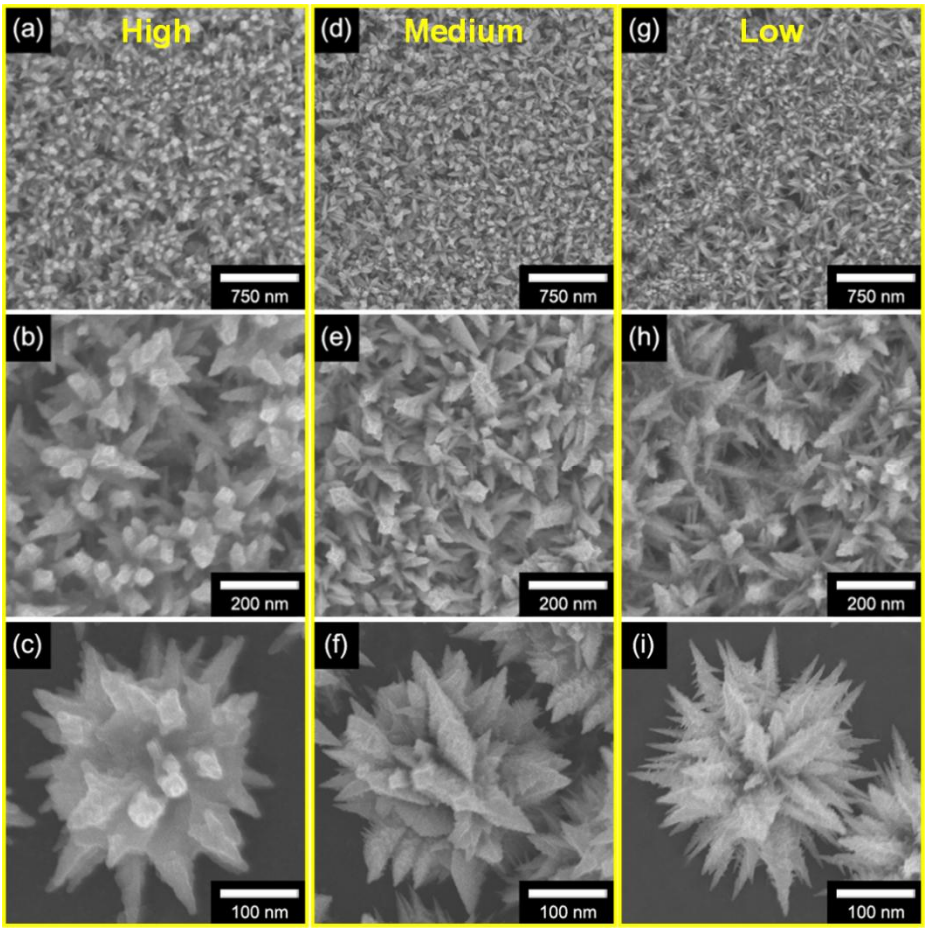

Figure 38. High, medium and low magnitude FE-SEM images of SPNFG with various sulfuric acid concentration in electrolyte solution; (a-c) 1 M, (d-f) 0.1 M, and (g-i) 0.01 M, respectively.

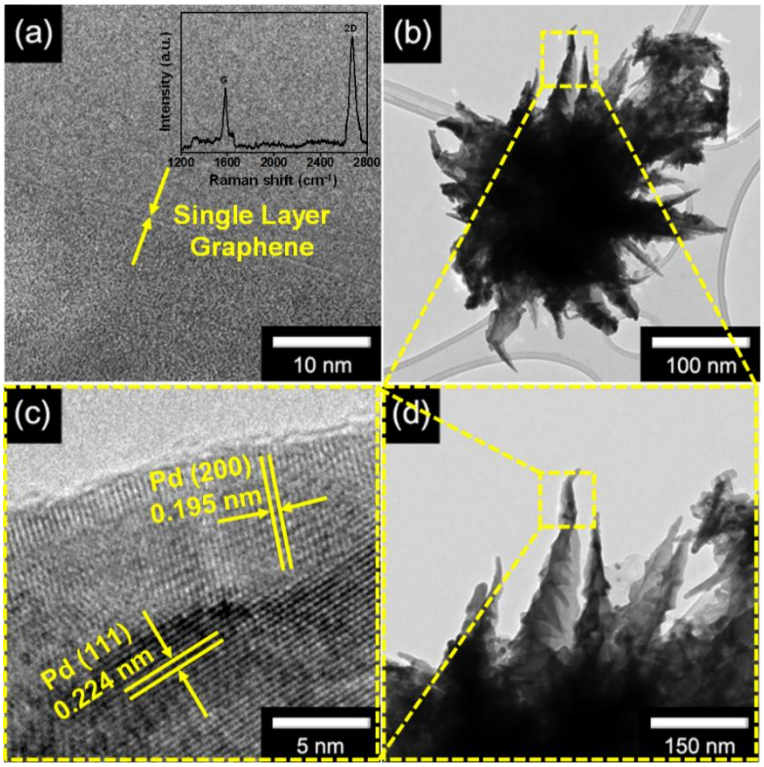

Figure 39. (a) High Resolution TEM (HR-TEM) image of single layer graphene, (b) low, (c) high, and (d) medium magnitude TEM images of PNF, respectively.

3.3.2. Characterization of sharpness-controlled PNFG

The chemical composition of the SPNFG was studied using X-ray Photoelectron Spectroscopy (XPS). The fully scanned spectra displays that only carbon and oxygen are presented in CVD graphene, while DAN-treated graphene has additional nitrogen peak from amino group in DAN. The two Pd peaks are observed in SPNFG with reducing nitrogen peak (**Figure 40a**). The highresolution XPS spectra of the C 1s peaks at *ca.* 285 eV region presents in **Figure 40b**. This peak is deconvoluted into four individual components as follows: the first peak for *ca.* 284.5 eV is assigned to sp^2-hybridized carbon atoms; the second peak for *ca.* 285.3 eV is attributed to a sp^3 carbon configuration; the third peak for *ca.* 286.4 eV is indexed to a sp^3 carbon atoms bonded to nitrogen or oxygen; and the last peak for *ca.* 288.6 eV is assigned to sp^2 carbon atom bonded to oxygen. Compared to CVD graphene, the peak of *ca.* 286.4 eV is almost maintained in DAN-treated CVD graphene due to the replacement from C-O to C-N, however, it is considerably decreased in PNFG owing to the decoration of PNFs on the graphene surface. **Figure 40c** shows the high-resolution N 1s spectrum of a SPNFG. Two components are observed at 399.2 and 400.6 eV for the amino N and pyrrolic N species of the DAN structure, respectively.

DAN-treated graphene has a major amino N peak owing to the amino group ($-NH_2$) by functionalization of DAN, whereas CVD graphene is nitrogen-free. Furthermore, the amino N peak for the PNFG is considerably decreased on account of the elimination of unreacted DAN during the washing process after electrodeposition. The Pd 3d peak consisted of two intense peaks and two weaker peaks, which are attributed to Pd^0 and Pd^{2+}, respectively (**Figure 40d**). The XPS study thus confirms that Pd^{2+} ions are successfully reduced to Pd^0 rather than PdO.

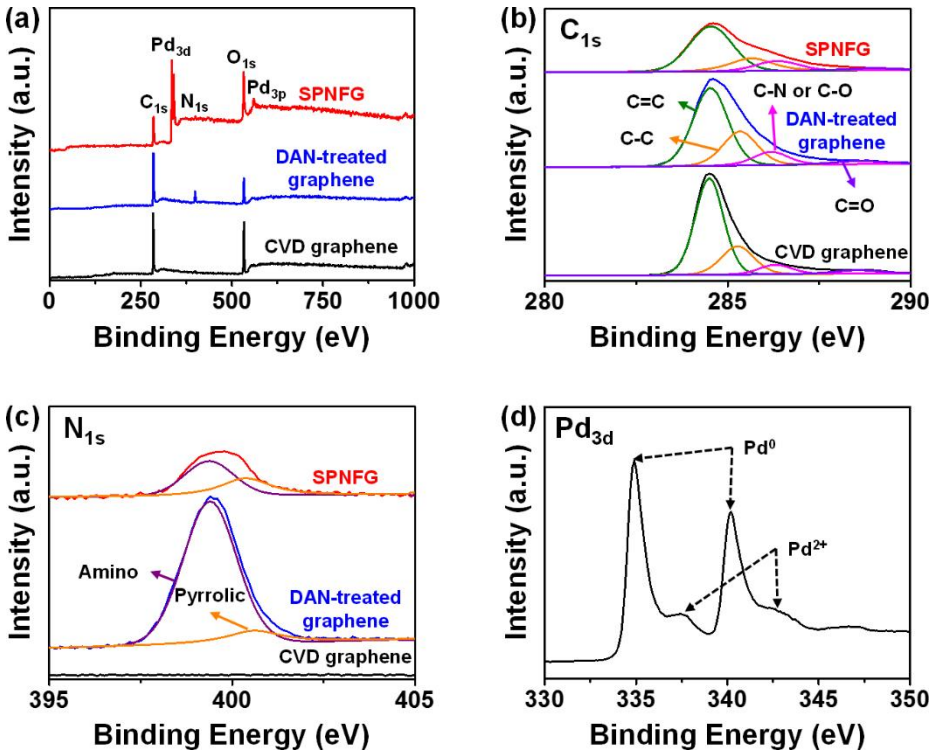

Figure 40. XPS patterns of (a) fully scanned spectra and (b) C 1s, (c) N 1s, and (d) Pd 3d of CVD graphene (black), DAN-treated graphene (blue), and SPNFG (red), respectively.

3.3.3. Fabrication of sharpness-controlled SPNFG sensor electrode

The stability between substrate and materials in a liquid-iongated sensor is an important consideration for the fabrication of a highly sensitive FET-type nonenzymatic sensor electrode. **Figure 41** is a schematic diagram of the fabrication procedure for the SPNFG based nonenzymatic FET-type sensor electrode. First, the CVD graphene surface was treated with 1,5-diaminonaphthalate (DAN) to functionalize with amino group (-NH_2). Afterward, PNFs were decorated by reduction of palladium ions combined with amino groups. The amine group of DAN on the graphene surface and sulfate ions in the electrolyte facilitates the formation of PNF structures. Two gold electrodes were deposited on the SPNFG through evaporation process. As a result, the SPNFG was pre-formed FET-type sensor electrode with 1 M NaOH (sodium hydroxide) as oxidation agent in PBS (phosphate-buffered saline) solution as the gate controller. In the FET-type electrode configuration, the two gold patterns on each side are the source (*S*) and drain (*D*), and the top gate electrode is placed in the electrolyte. The gate voltage (V_G) was applied to the source electrode in the 1M NaOH/PBS solution, and the distance between the electrode and gate was maintained at 2 mm.

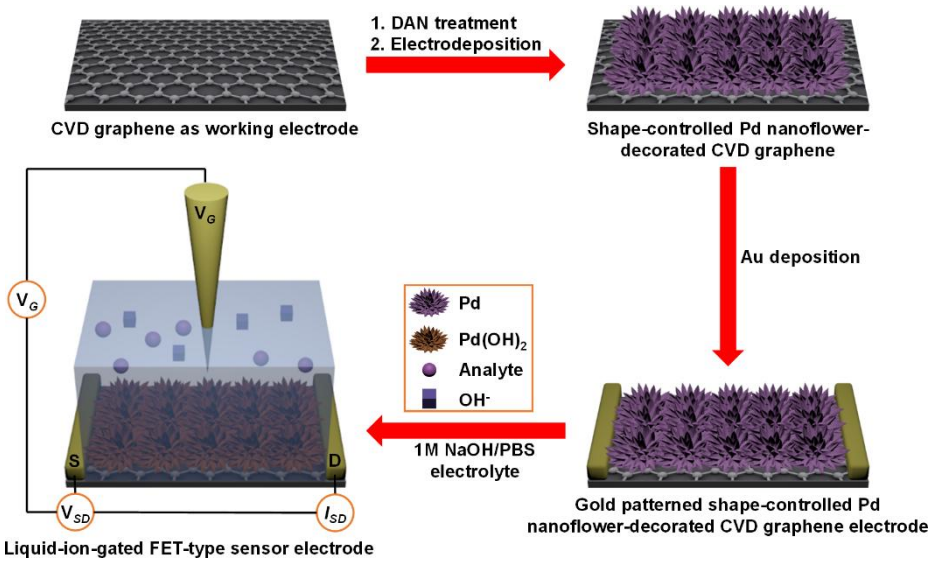

Figure 41. Illustrative diagram of the liquid-ion-gated FET-type sensor electrode with SPNFG.

3.3.4. Electrical properties of sharpness-controlled SPNFG electrode

A current-voltage (*I-V*) analysis was conducted to investigate the SPNFG electrical behavior. **Figure 42a** presents the I_{SD}-V_{SD} characteristics (V_G = 0) of pristine graphene and various SPNFGs. Due to the direct decoration of Pd, all of the electrode demonstrated the linear behavior of ohmic contacts in the voltage range from -1 to 1 V. This contrasts with the non-linear behavior of schottky barriers having poor electrical contacts. Moreover, the *dI/dV* value (conductivity) of the SPNFG considerably increased compared with the pristine graphene, due to the improved conductivity by PNF. **Figure 42b** represents the I_{SD}-V_{SD} plots of SPNFGs at various gate voltages (V_G) in steps of -0.1 V at a constant scan rate (10 mV s^{-1}). The I_{SD} decreased with decreasing V_G, which indicated p-type (major carrier: hole) behavior; this was attributed to oxygen-containing functional groups. Nevertheless, the linearity (*i.e.*, ohmic contact) is retained, implying that the V_G only influenced electrical current changes in the FET-type device.

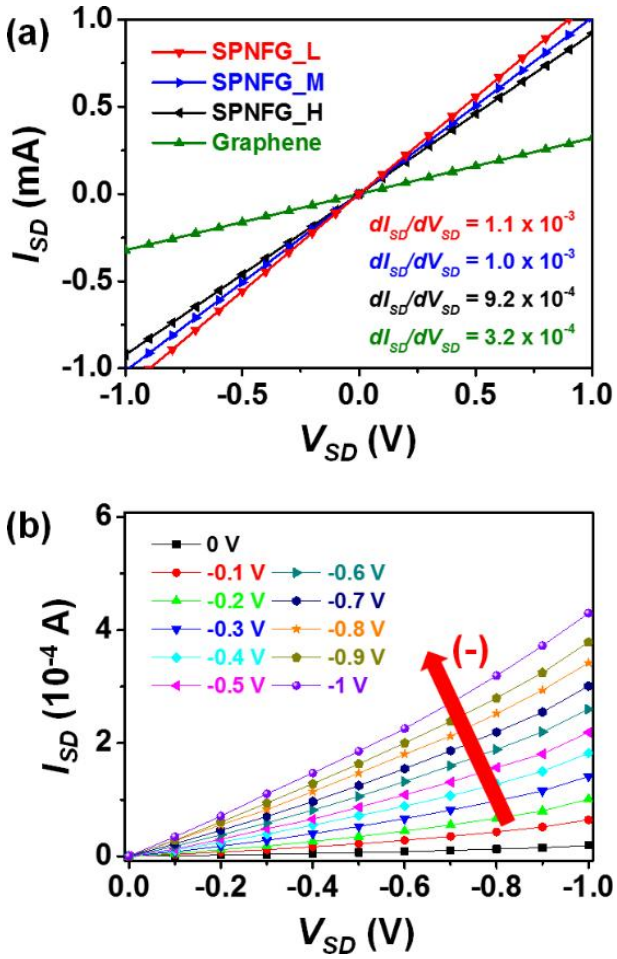

Figure 42. (a) Source-drain current voltage (I_{SD}-V_{SD}) curves of graphene (green), SPNFG_H (black), SPNFG_M (blue), and SPNFG_L (red), respectively. (b) I_{SD}-V_{SD} output characteristic of SPNFG liquid-ion-gated FET-type sensor with different gate voltage (V_G) from 0 to -1 in step of -0.1 V. (scan rate of V_{SD}: 10 mV s^{-1})

3.3.5. Real-time response of FET-type glucose sensor based on sharpness-controlled SPNFG electrode

A FET-type sensor is operated by measuring the density changes of the carrier. **Figure 43** describes the diagram of glucose detection mechanism using an FET-type SPNFG sensor electrode in the liquid-ion-gated system with 1M NaOH/PBS.

$Pd(OH)^2$ + glucose → Pd +gluconolactone + H_2O

$Pd + 2OH^- \rightarrow Pd(OH)_2 + 2e^-$

When the glucose adds on the SPNFG electrode, the palladium hydroxide ($Pd(OH)_2$) which is pre-formed by the NaOH is reduced to palladium (Pd). Then, reduced Pd is re-oxidized to $Pd(OH)_2$ with two electrons by ionization tendency, and these generated electrons transfer to the gate electrode, which changes the potential distribution to more negative. As a result, the density of the major carrier (hole) in the conducting channel increased, leading to the current increase while the resistance decreases. The I_{SD} was monitored at a V_G of -100 mV (V_{SD} = 1 mV) to examine the sensing characteristic of the liquid-ion-gated SPNFG FET-type electrode [153,154]. **Figure 44a** represents the real-time response of the SPNFG FET-type sensor with various shape as a function of glucose concentration. According to the addition of glucose,

the I_{SD} exhibits the increasing tendency due to the more negative gate voltage caused by the generated electrons. Furthermore, the response time for saturation increases with decreasing glucose concentration. It is difficult to achieve the threshold hole density to change the current at low concentration. The detection limit of the SPNFG FET-type sensor toward glucose is 1 nM for SPNFG_L at room temperature. This implies that SPNFG_L has many active sites which can react with glucose, and thereby drive the gate voltage becomes more negative. Moreover, the SPNFG FET-type sensor has a much lower detection limit than that of previously reported metal-carbon composite based nonenzymatic glucose sensors (**Table 2**). **Figure 44b** presents the sensitivity (S) as a function of glucose concentration. The S was measured as the difference between the addition and saturation points of the normalized current change ($[\Delta\ I/I0]_{SD}$ x 100), measured 20 s after glucose addition. The SPNFG FET-type sensor displayed linear behavior over a wide concentration range (10^{-9} M – 10^{-6} M), opposite as non-linear behavior at low concentrations (< 10^{-9} M). The outstanding advantage of the FET-type nonenzymatic sensor is robustness toward repetitive use. **Figure 45** represents the durability of the FET-type nonenzymatic sensor based on various SPNFGs at an

interval of 5 days. The durability was assessed as follows; the SPNFG electrode was placed in a sealed vessel at room temperature until each appointed date. The real-time response was then measured for a 1 x 10^{-6} M glucose concentration. The sensitivity remained high even after a long time.

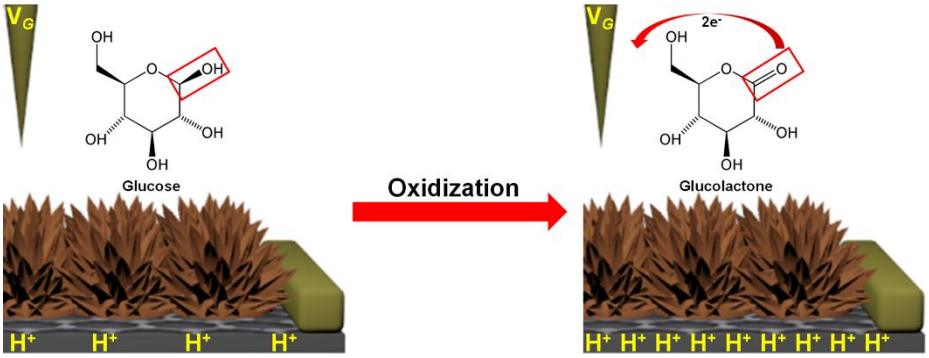

Figure 43. Schematic diagram of glucose sensing mechanism of SPNFG based on nonenzymatic FET-type sensor.

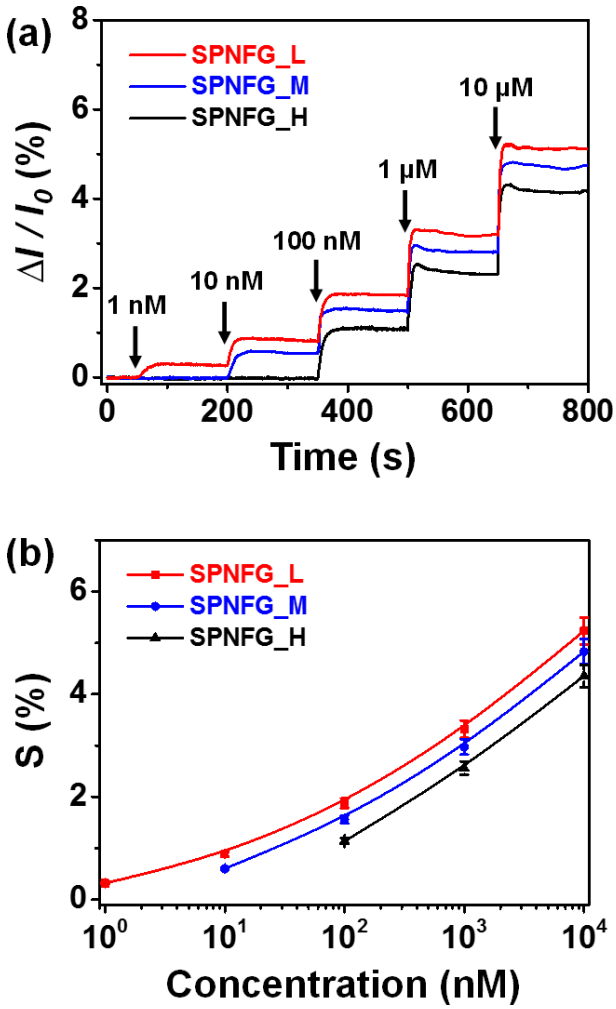

Figure 44. (a) Real-time response for the FET-type sensor with normalized current change ($\Delta I/I_0$ = $(I-I_0)/I_0$, where I_0 is the initial current and I is the instantaneous current). (b) Calibration curves of sensitivity of SPNFG as a function of glucose concentration.

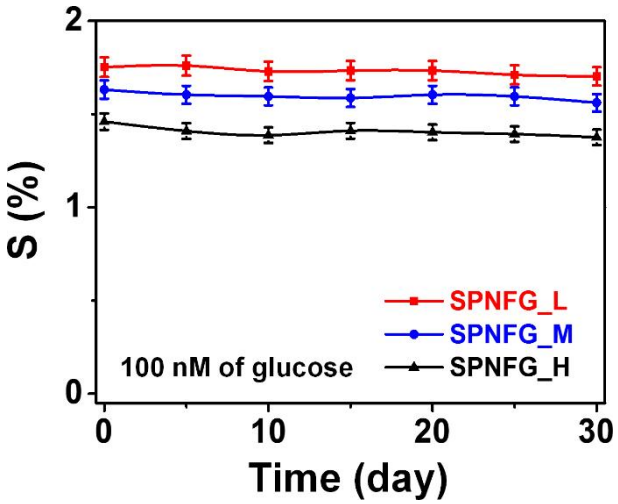

Figure 45. Durability test of SPNFG at an interval of 5 days consisting of SPNFG_H (black), SPNFG_M (blue), and SPNFG_L (red).

Table 2. Detection limits of non-enzyme glucose sensor based on noble metal/carbon composite.

Materials	Detection Limits	Linear range	Reference
SPNFG_L	1 nM	1 nM – 1 mM	This work
Pt/GOH[a)]	5 mM	5 – 20 mM	155
Pd-SWNT[b)]	0.2 μM	0.2 – 17 mM	156
Pd NPs/GO[c)]	0.2 mM	0.2 – 10 mM	157
Pt/MCs[d)]/GCE[e)]	28 μM	5 μM – 7.5 mM	158
Pt nanoflowers /GO/GCE	2 μM	2 μM – 10.3 nM	159

a) GOH, 3D graphene hydrogel; b) SWNT, single wall nanotube; c) GO, graphene oxide; d) MCs, mesoporous carbons; e) GCE, glassy carbon electrode.

3.3.6. Selectivity-improved FET-type glucose sensor

The selectivity of the SPNFG FET-type sensor toward glucose was observed for other biomolecules: uric acid and ascorbic acid. As shown in **Figure 46**, SPNFG FET-type sensor presents the considerable response to uric and ascorbic acid due to the similar detection mechanism (catalytic reaction). To enhance the selectivity toward glucose, glucose oxide (GOx)/graphene oxide (GO) and nafion/reduced graphene oxide (rGO) layers introduced into a step-by-step on the SPNFG surface using spin-coating method (**Figure 47**). Nafion composed of a Teflon backbone and acidic sulfonic group is negative charged and prevents the passing of the anionic electro-active molecules (uric acid and ascorbic acid) by electrostatic interaction. Moreover, glucose molecules couldn't pass through the nano-sized nafion layer [160,161]. On the other hand, the small size H_2O_2 which generated from reaction between glucose and GOx can contact with Pd.

$$\text{glucose} + \text{GOx} \rightarrow \text{gluconic acid} + H_2O_2 \quad (3)$$

These H_2O_2 molecules put the free electron by catalyst reaction as below proposed reaction.

$$H_2O_2 \rightarrow O_2 + 2H^+ + 2e^- \quad (4)$$

As a result, generated electron transfer to gate electrode, and the current increases due to the more negative gate voltage. Furthermore, numerous functional group in GO bonded with GOx, and, ring structure induced immobilization of GO in nafion layer by π –π interaction. The SPNFG coated with nafion was denoted as Nafion/SPNFG and the GOx immobilized Nafion/SPNFG was denoted as GOx/Nafion/SPNFG, respectively.

Figure 48 exhibits the real-time response of the Nafion/SPNFG_L FET-type sensor with uric and ascorbic acid. No reaction can be confirmed owing to the charge repulsion and size hindrance of protective film (nafion). On the other hand, GOx/Nafion/ SPNFG_L FET-type sensor presents the high selectivity toward glucose as explained mechanism (**Figure 49**). Accordingly, it can be concluded that liquid-ion gated FET-type sensor with high selectivity and sensitivity fabricated, successfully.

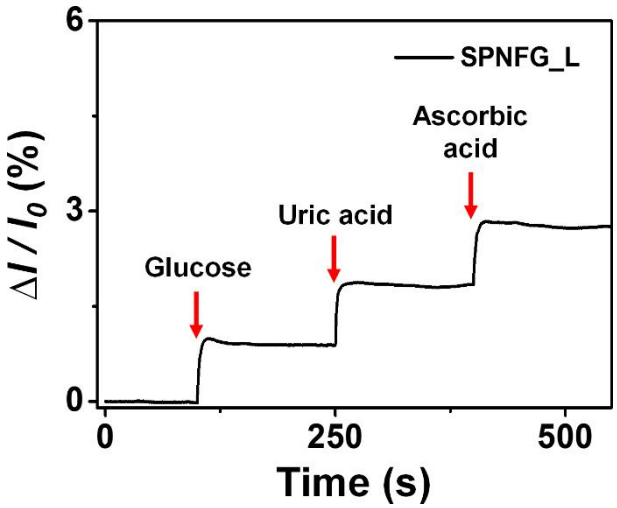

Figure 46. Real-time response for the FET-type sensor using SPNFG_L with normalized current change toward target and non-target molecule.

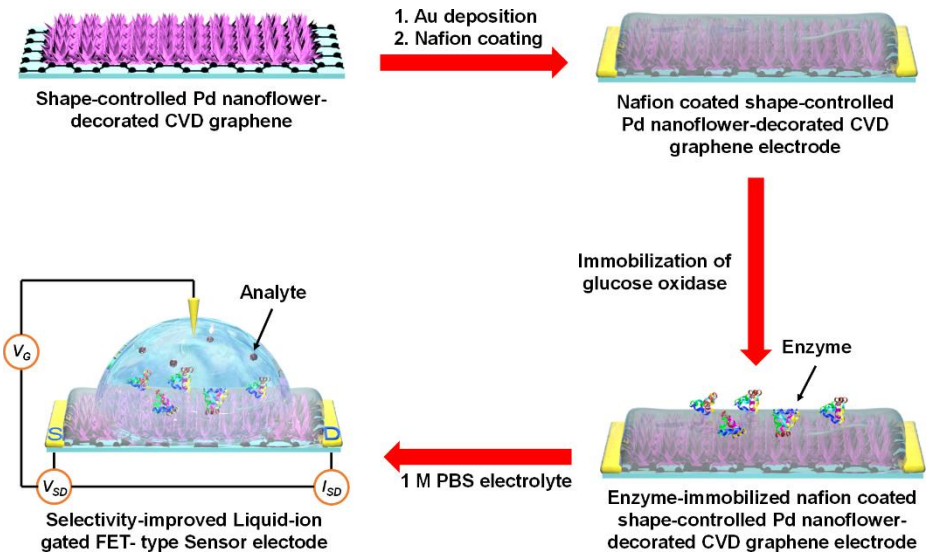

Figure 47. Illustration of fabrication procedure for the selectivity-improved liquid-ion-gated FET-type sensor electrode with SPNFG.

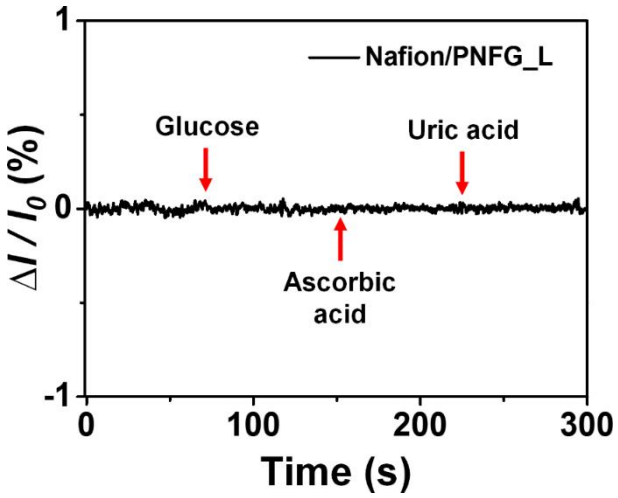

Figure 48. Selectivity responses of the Nafion/PNFG_L-based sensor toward non-target (ascorbic acid and uric acid) and target (glucose) analytes.

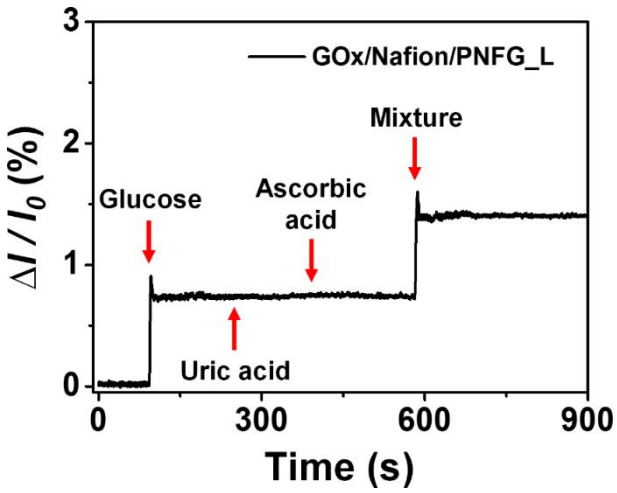

Figure 49. Real-time responses of the GOx/Nafion/PNFG_L based sensor toward non-target (ascorbic acid and uric acid), target (glucose), and mixture analytes.

4. Conclusion

The various variable-controlled including shape, population and sharpness palladium nanoflower-decorated composite materials were fabricated by CVD (chemical vapor deposition), electrospinning and electrodeposition methods and as-prepared materials displayed promising properties in the application areas of sensor. The subtopic is concluded in the view point of each subtopic as follows:

1. The shape-controlled palladium nanoparticles-decorated polypyrrole /polyacrylonitrile nanofibers (Pd_PPy/PAN NFs) were synthesized *via* electrospinning, vapor deposition polymerization (VDP), and electro-deposition process. One-dimensional PAN NFs act as substrate with high surface area to fabricate the conductive support for electrodeposition technique. Furthermore, the Pd shape was controlled by the amount of sulfate ion in electrolyte aqueous solution by hindering effect. Pd_PPy/PAN NFs-based FET-type sensor electrode were introduced as the transducer materials for detecting the hydrogen peroxide (H_2O_2) at room temperature. These FET-type H_2O_2 sensor exhibits a minimum detectable level (MDL) of 1 nM owing to not only a large amount of electrodeposited Pd by high surface area of PAN NFs

but also the increasing active sites for interaction by more pointed Pd. Therefore, this research illustrated a facile method for the fabrication of shape-controlled metal-conducting polymer composites for highly sensitive biosensor applications.

2. Flower-like palladium nanoclusters (FPNCs) are electrodeposited on CVD graphene (FPNCs_CG) electrode. The shape and population of FPNCs can be controlled by modifying the graphene surface with DAN. The phenyl groups of DAN interact with the graphene surface v*ia* $\pi - \pi$ interactions. The amino groups of DAN bind with Pd^{2+} ions to form Pd nanoparticles that act as nucleation sites. These sites, and the hindering effects of sulfate ions, resulted in the growth of FPNCs on the graphene surface. Transferring the CVD graphene film onto PEN substrates provide sensor films with excellent flexibility and desirable mechanical properties. The FPNCs_CG electrode are used as the signal-transducing element in hydrogen gas sensors at room temperature. The sensitivity and response time of these sensors improve with increasing FPNCs population. In particularly, the FPNCs_CG_H electrode has a minimum detectable level (MDL) of 0.1 ppm H_2. This report describes an effective method for the fabrication of flower-like metal-graphene

composites with population control for various flexible electrochemical applications.

3. A SPNFG-based FET-type nonenzymatic glucose sensor electrode was manufactured by surface modification and electrodeposition. To the best of our knowledge, this is the first demonstration of the fabrication of a metal-graphene composite based FET-type nonenzymatic sensor. The PNF that formed during the electrodeposition process, resulted from a hindering effect of sulfate ions in the electrolyte. The shape of the PNF was modulated by the concentration of sulfuric acid in the electrolyte solution. A FET-type nonenzymatic electrode using as-prepared SPNFG could detect glucose with high sensitivity and durability (1 month) at room temperature. Enhanced sensitivity (1 nM) was observed with more pointed morphology (SPNFG_L) because it reacted with more active site to interact with the analyte. Its sensitivity also correlated with differences of glucose concentration in saliva. Furthermore, selectivity was improved by introducing the protective layer. Accordingly, this research demonstrated an efficient method to fabricate a highly sensitive FET-type nonenzymatic sensors based on decoration of

nanoflower shape metal particles on a conductive composite material.

In summary, two types of carbon-derivative materials was adopted to conductive substrate for deposition of flower-like palladium nano-structure. First, polypyrrole-coated polyacrylonitrile nanofibers (PPy/PAN NFs), one-dimensional nanostrucrue, were fabricated via electrospinning and vapor deposition polymerization. Second, graphene, two dimensional carbon thin film, was prepared using chemical vapor deposition (CVD) technique. Then, palladium nanostructure was decorated these as-synthesized conductive substrate by electrodeposition method. Specially, surface modification of CVD graphene using treatment of diamino naphthalate (DAN) enable the control of flower-like Pd population. In addition, growth of palladium can be controlled by hindering effect of sulfate ion in electrolyte. These fabricated hybrid materials exhibited improved performance in the chemical/bio sensor application owing to the increasing active site as mentioned above. Moreover, these hybrid materials also can offer the application possibility such as catalyst, biotherapy, energy storage, *etc*.

References

[1] M. A. Memon, W. Bai, J. Sun, M. Imran, S. N. Phulpoto, S. Yan, Y. Huang, J. Geng, *ACS Appl. Mater. Interfaces* **2016**, 8, 11711.

[2] J. Jang, *Adv. Polym. Sci.* **2006**, 199, 189.

[3] C. Li, H. Bai, G. Shi, *Chem. Soc. Rev.* **2009**, 38, 2397.

[4] A. J. Heeger, *Angew. Chem. Int. Ed.* **2001**, 40, 2591.

[5] A. G. MacDiarmid, *Angew. Chem. Int. Ed.* **2001**, 40, 2581.

[6] C. M. Hangarter, N. Chartuprayoon, S. C. Hernandez, Y. Choa, N. V. Myung, *Nano Today* **2013**, 8, 39.

[7] Y. Jiang, C. Hu, H. Cheng, C. Li, T. Xu, Y. Zhao, H. Shao, L. Qu, *ACS Nano* **2016**, 10, 4735.

[8] J. Jang, J .H. Oh, X. L. Li, *J. Mater. Chem.* **2004**, 14, 2872.

[9] Y. Berdichevsky, Y-H. Lo, *Adv. Mater.* **2006**, 18, 122.

[10] P. Camurlu, *RSC Adv.* **2014**, 4, 55832.

[11] M. Zhou, M. Pagels, B. Geschke, J. Heinze, *J. Phys. Chem. B* **2002**, 106, 10065.

[12] Y. Huang, H. Li, Z. Wang, M. Zhu, Z. Pei, Q. Xue, Y. Huang, C. Zhi, *Nano Energy* **2016**, 22, 422.

[13] X. Yang, Z. Lin, J. Zheng, Y. Huang, B. Chen, Y. Mai, X. Feng, *Nanoscale* **2016**, 8, 8650.

[14] T. V. Vernitskaya, *Russ. Chem. Rev.* **1997**, 5, 443.

[15] X. Lu, W. Zhang, C. Wang, T. Wen, Y. Wei, *Prog. Polym. Sci.* **2011**, 36, 671.

[16] H. D. Tran, D. Li, R. B. Kanar, *Adv. Mater.* **2009**, 21, 1487.

[17] M. R. Abidian, D. Kim, D. C. Martin, *Adv. Mater.* **2006**, 18, 405.

[18] Z. Yin, Q. Zheng, *Adv. Energy Mater.* **2012**, 2, 179.

[19] Z. Huang, Y. Zhang, M. Kotaki, S. Ramakrishna, *Compos. Sci. Technol.*

2003, 63, 2223.

[20] N. Bhardwaj, S. C. Kundu, *Biotechnol. Adv.* **2010**, 28, 325.

[21] A. Akbarinejad, A. Ghoorchian, M. Kamalabadi, N. Alizadeh, *Sens. Actuators, B* **2016**, 236, 99.

[22] T. Subbiah, G. S. Bhat, R. W. Tock, S. Parameswaran, S. S. Ramkumar, *J. Appl. Polym. Sci.* **2005**, 96, 557.

[23] Y. Xia, P. Yang, Y. Sun, Y. Wu, B. Mayers, B. Gates, Y. Yin, F. Kim, H. Yan, *Adv. Mater.* **2003**, 15, 353.

[24] Y. Zhang, L. Zhang, C. Zhou, *Acc. Chem. Res.* **2013**, 46, 2329

[25] M. J. Allen, V. C. Tung, R. B. Kaner, *Chem. Rev.* **2010**, 110, 132.

[26] M. Yang, Y. Hou, N. A. Kotov, *Nano Today* **2012**, 7, 430.

[27] K. S. Kim, Y. Zhao, H. Jang, S. Y. Lee, J. M. Kim, K. S. Kim, J. Ahn, P. Kim, J. Choi, B. H. Hong, *Nature* **2009**, 457, 706.

[28] S. J. Park, O. S. Kwon, S. H. Lee, H. S. Song, T. H. Park, J. Jang, *Nano Lett.* **2012**, 12, 5082.

[29] A. Reina, X. Jia, J. Ho, D. Nezich, H. Son, V. Bulovic, M. S. Dresselhaus, J. Kong, *Nano Lett.* **2009**, 9, 30.

[30] D. Wei, Y. Liu, Y. Wang, H. Zhang, L. Huang, G. Yu, *Nano Lett.* **2009**, 9, 1752.

[31] S. K. Konda, A. Chen, *Mater. Today* **2016**, 19, 100.

[32] Y. Pak, S. Kim, H. Jeong, C. G. Kang, J. S. Park, H. Song, R. Lee, N. Myoung, B. H. Lee, S. Seo, J. T. Kim, G. Jung, *ACS Appl. Mater. Interfaces* **2014**, 6, 13293.

[33] J. Li, T. Zhao, T. Chen, Y. Liu, C. N. Oug, J. Xie, *Nanoscale* **2015**, 7, 7502.

[34] X. Xu, Y. Li, Y. Gong, P. Zhang, H. Li, Y. Wang, *J. Am. Chem. Soc.* **2012**, 134, 16987.

[35] A. Kolmakov, D. O. Klenov, Y. Lilach, S. Stemmer, M. Moskovits, *Nano Lett.* **2005**, 5, 667.

[36] A. Baldi, T. C. Narayan, A. L. Koh, J. A. Dionne, *Nat. Mater.* **2014**, 13, 1143.

[37] F. Yang, S. Kung, M. Cheng, J. C. Hemminger, R. M. Penner, *ACS Nano* **2010**, 4, 5233.

[38] X. Q. Zeng, M. L. Latimer, Z. L. Xiao, S. Panuganti, U. Welp, T. Xu, *Nano Lett.* **2011**, 11, 262.

[39] A. Tittl, P. Mai, R. Taubert, D. Dregely, N. Liu, H. Giessen, *Nano Lett.* **2011**, 11, 4366.

[40] F. Yang, D. K. Taggart, R. M . Penner, *Nano Lett.* **2009**, 9, 2177.

[41] D. Ding, Z. Chen, *Adv. Mater.* **2007**, 19, 1996.

[42] B. M. Novak, *Adv. Mater.* **1993**, 5, 422.

[43] C. Sanchez, B. Julian, P. Belleville, M. Popall, *J. Mater. Chem.* **2005**, 15, 3559.

[44] W. U. Huynh, J. J. Dittmer, A. P. Alivisatos, *Science* **2002**, 295, 2425.

[45] F. Caruso, R. A. Caruso, H. Mohwald, *Science* **1998**, 282, 1111.

[46] M. Hasik, A. Bernasik, A. Adamczyk, G. Malata, K. Kowalski, J. Camra, *Eur. Polym. J.* **2003**, 39, 1669.

[47] K. –M. Mangold, F. Meik, K. Juttner, *Synth. Met.* **2004**, 144, 221.

[48] A. Buoleghlimt, N. J. Buurma, *Langmuir* **2012**, 28, 2436.

[49] V. V. Kondratiev, V. V. Malev, S. N. Eliseeva, *Russ. Chem. Rev.* **2016**, 85, 14.

[50] A. Fahmi, T. Pietsch, C. Mendoza, N. Cheval, *Mater. Today* **2009**, 12, 44.

[51] L. Shang, T. Bian, B. Zhang, D. Zhang, L. Wu, C. Tung, Y. Yin, T. Zhang, *Angew. Chem. Int. Ed.* **2014**, 53, 250.

[52] Y. Kim, Y. Noh, E. J. Lim, S. Lee, S.M. Choi, W. B. Kim, *J. Mater. Chem. A* **2014**, 2, 6976.

[53]S. Yang, J. Dong, Z. Yao, C. Shen, X. Shi, Y. Tian, S. Lin, X. Zhang, *Sci. Rep.* **2014**, 4, 4501.

[54] D. Grujicic, B. Pesic, *Electrochim. Acta* **2002**, 47, 2901.

[55] A. P. Abbott, K. J. McKenzie, *Phys. Chem. Chem. Phys.* **2006**, 8, 4265.

[56] E. Herrero, L. J. Buller, H. D. Abruna, *Chem. Rev.* **2001**, 101, 1897.

[57] S. Peulon, D. Linco, *J. Electrochem. Sco.* **1998**, 145, 864.

[58] S. Peulon, D. Linco, *Adv. Mater.* **1996**, 8, 166.

[59] I. M. Dharmadasa, J. Halgh, *J. Electrochem. Soc.* **2006**, 153, G47.

[60] X. Huang, Z. Yin, S. Wu, X. Qi, Q. He, Q. Zhang, F. Bory, H. Zhang, *Small* **2011**, 7, 1876.

[61] A. N. Shipway, E. Katz, I. Willner, *ChemPhysChem* **2000**, 1, 18.

[62] J. Bai, B. Zhou, *Chem. Rev.* **2014**, 114, 10131.

[63] K. Saha, S. S. Agasti, C. Kim, X. Li, V. M. Rotello, *Chem. Rev.* **2012**, 112, 2739.

[64] H. Bai, G. Shi, *Sensors* **2007**, 7, 267.

[65] J. Homola, *Chem. Rev.* **2008**, 108, 462.

[66] Y. Shao, J. Wang, H. Wu, J. Liu, I. A. Aksay, Y. Lin, *Electroanalysis* **2010**, 22, 1027.

[67] J. Lee, *Sens. Actuators, B* **2009**, 140, 319.

[68] U. Lange, N. V. Roznyatovskaya, V. M. Mirsky, *Analytica. Chimica. Acta.* **2008**, 614, 1.

[69] L. E. Kreno, K. Leong, O. K. Farha, M. Allendorf, R. P. V. Duyne, J. T. Hupp, *Chem. Rev.* **2012**, 112, 1105.

[70] S. W. Thomas III, G. D. Joly, T. M. Swager, *Chem. Rev.* **2007**, 107, 1339.

[71] A. Kolmakov, M. Moskovits, *Ann. Rev. Mater. Res.* **2004**, 34, 151.

[72] Y. Liu, X. Dong, P. Chen, *Chem. Soc. Rev.* **2012**, 41, 2283.

[73] W. Lubitz, W. Tumas, *Chem. Rev.* **2007**, 107, 3900.

[74] W. Grochala, *Nat. Chem.* **2015**, 7, 264.

[75] G. Korotcentkov, S. D. Han, J. R. Stteter, *Chem. Rev.* **2009**, 109, 1402.

[76] T. Hubert, L. B. Brett, G. Black, U. Banach, *Sens. Actuators, B* **2011**, 157, 329.

[77]D. Yang, I. Kamienchick, D. Y. Youn, A. Rothschild, I. Kim, *Adv. Funct. Mater.* **2010**, 20, 4258.

[78] B. Wang, L. F. Zhu, Y. H. Yang, N. S. Xu, G. W. Yang, *J. Phys. Chem. C* **2008**, 112, 6643.

[79] H. Gu, Z. Wang, Y. Hu, *Sensors* **2012**, 12, 5517.

[80] B. K. Sharma, J. Ahn, *Solid State Electon.* **2013**, 89, 177.

[81] B. Zhan, C. Li, J. Yang, G. Jenkins, W. Huang, X. Dong, *Small* **2014**, 10, 4042.

[82]Q. He, H. G. Sudibya, Z. Yin, S. Wu, H. Li, F. Boey, W. Huang, P. Chen, H. Zhang, *ACS Nano* **2010**, 4, 3201.

[83] X. You, J. J. Pak, *Sens. Actuators, B* **2014**, 202, 1357.

[84] Y. Lee, S. Bae, H. Jang, S. Jang, S. Zhu, S. H .Sim, Y. II. Song, B. H. Hong, J. Ahn, *Nano Lett.* **2010**, 10, 490.

[85] Y. H. Kwak, D. S. Chio, Y. N. Kim, H. Kim, D. H. Yoon, S. S. Ahn, J. W. Yang, W. S. Yang, S. Seo, *Biosens. Bioelecton.* **2012**, 37, 82.

[86] X. Yang, Y. Ouyang, F. Wu, Y. Hu, Y. Ji, Z. Wu, *Sens. Actuators, B* **2017**, 238, 40.

[87] H. Yoon, S. Ko, J. Jang, *J. Phys. Chem. B* **2008**, 112, 9992.

[88] C. Kuo, W. Lan, C. Chen, *Nanoscale* **2014**, 6, 334.

[89] H. Pang, Y. Zhang, T. Cheng, W. Lai, W. Huang, *Nanoscale* **2015**, 7, 16012.

[90] J. W. Park, S. J. Park, O. S. Kwon, C. Lee, J. Jang, *Anal. Chem.* **2014**, 86, 1822.

[91] R. Liu, S. Li, X. Yu, G. Zhang, S. Zhang, J. Yao, B. Keita, L. Nadjo, L. Zhi, *Small* **2012**, 8, 1398.

[92] D. Lu, J. Cardiel, G. Cao, A. Q. Shen, *Adv. Mater.* **2010**, 22, 2809.

[93] Y. Lu, M. Meyyappan, J. Li, *Small* **2011**, 7, 1714.

[94] J. Y. Zheng, Y. Yan, X. Wang, W. Shi, H. Ma, Y. S. Zhao, J. Yao, *Adv. Mater.* **2012**, 24, OP194.

[95] N. S. Oliver, C. Toumazou, A. E. G. Cass, D. G. Johnston, *Diabetic Med.* **2009**, 26, 197.

[96] A. Heller, B. Feldman, *Chem. Rev.* **2008**, 108, 2482.

[97] O. Veiseh, R. Lauger, *Nature* **2015**, 524, 39.

[98] M. F. Hossian, Y. Park, *Electroanalysis* **2014**, 26, 940.

[99] J. Wang, D. F. Thomas, A. Chem, *Anal. Chem.* **2008**, 80, 997.

[100] A. P. F. Turner, *Chem. Soc. Rev.* **2013**, 42, 3184.

[101] J. Wang, *Chem. Rev.* **2008**, 108, 814.

[102] S. Li, J. Chou, T. Sun, S. Hsiung, H. Shieh, *Sens. Lett.* **2011**, 9, 143.

[103] X. Wang, O. S. Wolfbeis, *Chem. Soc. Rev.* **2014**, 43, 3666.

[104] M. Steiner, A. Duerkop, O. S. Wolfbeis, *Chem. Soc. Rev.* **2011**, 40, 4805.

[105] H. Matsui, W. Badalawa, A. Ikeheta, H. Tabata, *Adv. Opt. Mater.* **2013**, 1, 397.

[106] A. Chen, S. Chatterjee, *Chem. Soc. Rev.* **2013**, 42, 5425.

[107] N. J. Ronkainen, H. B. Halsall and W. R. Heineman, *Chem. Soc. Rev.* **2010**, 39, 1747-1763.

[108] C. Chen, Q. Xie, D. Yang, H. Xiao, Y. Fu, Y. Tan and S. Yao, *RSC Adv.* **2013**, 3, 4473-4491.

[109] J. Liu, W. Lv, W. Wei, C. Zhang, Z. Li, B. Li, F. Kang and Q. Yang, *J. Mater. Chem. A* **2014**, 2, 3031-3037.

[110] S. Y. Cu, J. Ren, Q. L. Wu, *Synth. Met.* **2005**, 155, 157.

[111] E. Zussman, A. L. Yarin, A. V. Bazilevsky, R. Avrahami, M. Feldman, *Adv. Mater.* **2006**, 18, 348.

[112] J. J. Mak, L. M. Viculis, A. Ali, R. Luoh, G. Yang, H. T. Hahn, F. K. Ko, R. B. Kaner, *Adv. Mater.* **2005**, 17, 77.

[113] J. Jang, B. Lim, *Angew. Chem. Int. Ed.* **2003**, 42, 5600.

[114] J. S. Lee, D. H. Shin, J. Jun, C. Lee, J. Jang, *ChemSusChem* **2014**, 7, 1676.

[115] J. S. Lee, D. H. Shin, J. Jang, *Energy Environ. Sci.* **2015**, 8, 3030.

[116] J. S. Lee, D. H. Shin, W. Kim, J. Jang, *J. Mater. Chem. A* **2016**, 4, 6603.

[117] T. Hsieh, H. Chen, C. Kung, C. Wang, R. Vittal, K. Ho, *J. Mater. Chem.* **2012**, 22, 5550.

[118] Y. Lei, B. Liu, J. Lu, R. J. Lobo-Lapidus, T. Wu, H. Feng, X. Xia, A. U. Mane, J. A. Libera, J. P. Greeley, J. T. Miller, J. W. Elam, *Chem. Mater.* **2012**, 24, 3525.

[119] Y. Zhu, S. Murali, W. Cai, X. Li, J. W. Suk, J. R. Potts, R. S. Ruoff, *Adv. Mater.* **2010**, 22, 3906.

[120] H. Choi, J. S. Choi, J. Kim, J. Choe, K. H. Chung, J. Shin, J. T. Kim, D. Youn, K. Kim, J. Lee, S. Choi, P. Kim, C. Choi, Y. Yu, *Small* **2014**, 18, 3685.

[121] J. Lee, K. S. Novoselov, H. S. Shin, *ACS Nano* **2011**, 5, 608.

[122] X. Dong, D. Fu, W. Fang, Y. Shi, P. Chen, L. Li, *Small* **2009**, 5, 1422.

[123] S. K. Hong, S. M. Song, O. Sul, B. J. Cho, *J. Electrochem. Soc.* **2012**, 159, K107.

[124] X. Xie, G. Gao, Z. Pan, T. Wang, X. Meng, L. Cai, *Sci. Rep.* **2014**, 5, 8515.

[125] Y. Xiong, H. Cai, B. J. Wiley, J. Wang, M. J. Kim, Y. Xia, *J. Am. Chem. Soc.* **2007**, 129, 3665.

[126] Y. Xiong, H. Cai, Y. Yin, Y. Xia, *Chem. Phys. Lett.* **2007**, 440, 273.

[127] M. G. Campbell, D. C. Powers, J. Raynaud, M. J. Graham, P. Xie, E. Lee, T. Ritter, *Nat. Chem.* **2011**, 3, 949.

[128] B. Lim, Y. Xiong, Y. Xia, *Angew. Chem. Int. Ed.* **2007**, 46, 9279.

[129] A. Ponrouch, S. Garbarino, E. Bertin, C. Andrei, G. A. Botton, D. Guay, *Adv. Funct. Mater.* **2012**, 22, 4172.

[130] R. Dus, R. Nowakowski, E. Nowicka, *J. Alloys Compd.* **2005**, 404-406, 284.

[131] P. Grammatikopoulos, C. Cassidy, V. Singh, M. Sowwan, *Sci. Rep.* **2014**, 4, 5779.

[132] Y. Murata, E. Starodub, B. B. Kappes, C. V. Ciobanu, N. C. Bartelt, K. F. McCarty, S. Kodambaka, *Appl. Phys. Lett.* **2010**, 97, 143114.

[133] R. Dus, R. Nowakowski, E. Nowicka, *J. Alloys Compd.* **2005**, 404-406, 284.

[134] L. G. D. Arco, Y. Zhang, C. W. Schlenker, K. Ryu, M. E. Thompson, C. Zhou, *ACS Nano* **2010**, 4, 2865.

[135] R. S. Sundaram, C. Gomez-Navarro, K. Balasubramanian, M. Burghard, K. Kern, *Adv. Mater.* **2008**, 20, 3050.

[136] P. A. Pandey, N. R. Wilson, J. A. Covington, *Sens. Actuators, B* **2013**, 183, 478.

[137] U. Lange, T. Hirsh, V. M. Mirsky, O. S. Wolfbeis, *Electrochim. Acta.* **2011**, 56, 3707.

[138] M. Gautam, A. H. Jayatissa, *Solid-State Electron.* **2012**, 78, 159.

[139] N. Hu, Z. Yang, Y. Wang, L. Zhang, Y. Wang, X. Huang, H. Wei, L. Wei, Y. Zhang, *Nanotechnol.* **2014**, 25, 25502.

[140] H. Y. Jeong, D. Lee, H. K. Choi, D. H. Lee, J. Kim, J. Y. Lee, W. J. Lee, S. O. Kim, S. Choi, *Appl. Phys. Lett.* **2010**, 96, 213105.

[141] P. Su, H. Shieh, *Sens. Actuators, B* **2014**, 190, 865.

[142] B. Cho, J. Yoon, M. G. Haham, D. Kim, A. R. Kim, Y. H. Kahng, S. Park, Y. Lee, S. Park, J. Kwon, C. S. Kim, M. Song, Y. Jeong, K, Nam, H. C. Ko, *J. Mater. Chem. C* **2014**, 2, 5280.

[143] J. H. An, S. J. Park, O. S. Kwon, J. Bae, J. Jang, *ACS Nano* **2013**, 7, 10563.

[144] O. S. Kwon, S. R. Ahn, S. J. Park, H. S. Song, S. H. Lee, J. S. Lee, J. Hong, J. S. Lee, S. A. You, H. Yoon, T. H. Park, J. Jang, *ACS Nano*

2012, 6, 5549.

[145] O. S. Kwon, S. J. Park, J. Hong, A. Han, J. S. Lee, J. S. Lee, J. H. Oh, J. Jang, *ACS Nano* **2012**, 6, 1486.

[146] R. Garg, N. L Dutta, N. R. Choudhury, *Nanomaterials* **2014**, 4, 267.

[147] S. J. Park, O. S. Kwon, S. H. Lee, H. S. Song, T. H. Park, J. Jang, *Nano Lett.* **2012**, 12, 5082.

[148] J. L. Johnson, A. Behnam, S. J. Pearton, A. Ural, *Adv. Mater.* **2010**, 22, 4877.

[149] M. G. Chung, D. Kim, D. K. Seo, T. Kim, H. U. Im, H. M. Lee, J. Yoo, S. Hong, T. J. Kang, Y. H. Kim, *Sens. Actuators, B* **2012**, 169, 387.

[150] B. Zhan, C. Li, J. Yang, G. Jenkins, W. Huang, X. Dong, *Small,* **2014**, 10, 4042.

[151] Y. Zhang, L. Zhang, C. Zhou, *Acc. Chem. Res.* **2013**, 46, 2329.

[152] T. Hseieh, H. Chen, C. Kung, C. Wang, R. Vittal, K. Ho, *J. Mater. Chem.* **2012**, 22, 5550.

[153] D. H. Shin, J. S. Lee, J. Jun, J. H. Ahn, S. G. Kim, K. H. Cho, J. Jang, *Sci. Rep.* **2015**, 5, 12994.

[154] I. Heller, S. Chatoor, J. Mannik, M. A. G. Zevenbergen, C. Dekker, S. G. Lemay, *J. Am. Chem. Soc.* **2010**, 132, 17149.

[155] Y. Y. Wang, P. J. Burke, *Appl. Phys. Lett.* **2013**, 103, 052103-4.

[156] L. T. Hoa, K. G. Sun, S. H. Hur, *Sens. Actuators, B* **2015**, 210, 618.

[157] J. Meng, J. Jin, G. Yang, T. Lu, H. Zhang, C. Cai, *Anal. Chem.* **2009**, 81, 7271.

[158] Q. Wang, X. Cui, J. Chen, X. Zheng, C. Liu, T. Xue, H. Wang, Z. Jin, L. Qiao, W. Zheng, *Appl. Phys. Lett.* **2013**, 103, 052103-4.

[159] C. Su, C. Zhang, G. Lu, C. Ma, *Electroanalysis* **2010**, 22, 1901.

[160] G. Wu, X. Song, Y. Wu, X. Chen, F. Luo, X. Chen, *Talanta* **2013**, 105, 379.

[161] C. Liao, C. Mak, M. Zhang, H. L. W. Chan, F. Yan, *Adv. Mater.* **2015**,

27, 676.

국문초록

재료 공학 분야에서 우수한 물성과 성능을 보이는 새로운 물질의 개발이 활발히 진행되고 있다. 특히, 무기물과 유기물이 융합된 복합재료는 높은 성능의 무기물과 높은 안전성의 유기물이 시너지 효과를 일으켜 물성이나 성능뿐만 아니라 경제적, 환경적 요구까지 충족시킴으로써 많은 연구가 진행되고 있다. 그 중에서도 팔라듐을 포함하는 탄소기반 복합재료는 수소와의 반응성과 높은 촉매 성능으로 인해 많은 학업 및 산업 분야에서 관심을 받고 있다. 하지만, 필러로써 무기물 나노 물질을 제조하여 단순히 혼합하는 개념 (blend, mixture)의 복합나노재료는 많이 응용되고 있으나, 박히거나 표면에 도입되는 개념 (embedding, decoration) 의 제조 연구는 미진한 실정이다.

본 학위 논문에서는 전도성 지지체로써 전기방사와 기상증착중합 (vapor deposition polymerization)을 이용한 폴리피롤/폴리아크릴로나이트릴 나노섬유와 화학기상증착(chemical vapor deposition)을 이용한 탄소 박막을 제조하고 전기도금법 (electrodeposition) 방법을 이용해

팔라듐을 도입하는 복합재료는 향상된 전기적/화학적 특성들을 보여주며, 다양한 센서분야에 활용 할 수 있게 한다. 이렇게 제조된 금속과 탄소기반의 복합재료는 시너지 효과로 인해 센서의 전달체로써 도입되었을 때, 빠른 응답속도와 안정성을 제공한다. 또한, 조절된 팔라듐 구조체로 인한 넓은 표면적은 목표물질과의 증폭된 상호작용을 야기함으로써 고감도의 센서 구현을 가능하게 한다.

주요어: 팔라듐, 폴리피롤, 그래핀, 전계-효과 트랜지스터, 센서

학 번: 2014-30255